Joint Mapping of Chromatin Accessibility and Targeted Proteomics in HER2-expressing Breast Cancer Systems

Anna Fomitcheva Khartchenko*, Trinh Lam*, Nadine Goldhammer, Marin Bont, Shruti Warhadpande, Jennifer M. Rosenbluth, and Amy E. Herr

* Equal contribution

Keywords
Multiomics, HER2, patient-derived organoids (PDOs), ATAC-seq, chromatin accessibility, single-cell western blot

Highlights

- To evaluate the impact of chromatin accessibility on HER2 proteoform expression, we introduce EpiBlot, a novel workflow combining a plateATAC-seq assay (i.e., mini-96 well-plate requiring 5-500 nuclei) with single-cell Western blot.
- Increased chromatin accessibility and significantly larger nuclei were detected in a breast cancer cell line (MCF7) engineered to express the truncated HER2 proteoform (611-CTF) versus a line expressing only the full-length HER2 protein.
- Lapatinib-targeted treatment did not induce widespread changes in chromatin accessibility.
- Doxorubicin reshapes chromatin accessibility in HER2-proteoform cell lines, producing both gains and losses across the genome.
- Chromatin accessibility and protein abundance are moderately correlated, with a wide range of protein abundance measured across single cells.
- HER2-low patient-derived breast cancer organoids exhibit decreased accessibility in the ERBB2 region despite increased HER2 protein expression, as compared to normal breast cells.

Summary
HER2 proteoforms promote therapeutic resistance and aggressiveness in HER2-positive breast cancer, yet their epigenetic consequences remain poorly defined. Here, we establish EpiBlot, a joint assay incorporating a customized plateATAC-seq workflow that minimizes sample inputs with single-cell western blotting to concurrently profile chromatin accessibility with protein and proteoform expression in breast cancer MCF7 cells. Engineered MCF7 cells expressing HER2 proteoforms - full-length p185HER2 or truncated 611-CTF - were evaluated on the impact of such proteoforms after lapatinib or doxorubicin exposure. Expression of 611-CTF elicits pervasive chromatin remodeling, whereas p185HER2 provokes only modest accessibility shifts under the same treatments. Lapatinib treatment produces limited global effects but unmasks proteoform-specific responses, while treatment with doxorubicin drives extensive genome-wide accessibility changes. Concordance between chromatin accessibility and protein abundance is moderate, underscoring complex regulatory coupling. Extending this dual-modality approach to HER2-low patient-derived organoids uncovers distinct chromatin states and reveals a subpopulation of triple-negative breast-cancer cells expressing truncated HER2 proteoforms. These findings highlight the value of multimodal profiling with proteoform identification for dissecting tumor heterogeneity and therapeutic response in HER2-positive breast cancer.

Graphical abstract

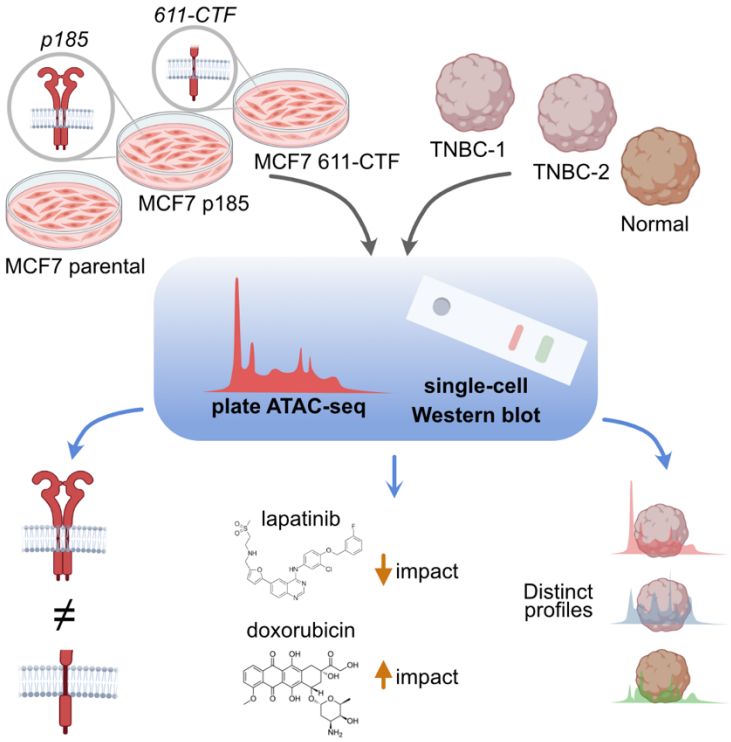

Introduction

Female breast cancer was the second most commonly diagnosed cancer worldwide in 2022[1]. Among the subtypes of breast cancer, HER2+ accounts for up to 20% of all cases[2]. HER2 (human epidermal growth factor receptor 2) is a membrane-bound receptor that can form homodimers and heterodimers with other members of the Early Growth Response (EGR) family[3]. The signaling cascades downstream of HER2 regulate essential cell functions such as cell differentiation, proliferation, adhesion, and migration[3]. HER2 as a target for anti-cancer therapy remains a major focus of preclinical investigation[4]. Current anti-HER2 cancer therapies include monoclonal antibodies against the extracellular domain of HER2 (e.g., trastuzumab or pertuzumab) and small molecule inhibitors targeting the HER2 tyrosine kinase domain (e.g., lapatinib, neratinib, or tucatinib)[3]. While these treatments have been traditionally indicated for tumors with HER2 overexpression (HER2+ or HER2-amplified tumors), recent clinical advances show that patients with immunohistochemistry score of +1, or +2 with negative *in situ* hybridization for HER2, namely HER2-low or even HER2-ultralow tumors, can benefit from HER2-directed therapy, such as the antibody-drug conjugate trastuzumab-deruxtecan[5]. This emerging clinical category may represent a group with distinct biology that still remains under investigation[6,7].

Multiple causes for therapeutic resistance in HER2+ cancers exist, including the expression of HER2 proteoforms. These proteoforms are altered forms of the full-length HER2 protein that include carboxy-terminus fragments (CTFs), splicing variants, and mutations. Select HER2 proteoforms have been explored for their impact in tumor progression and response to treatment. These are the d16HER2 splice variant, which results from the skipping of exon 16 during

transcription, as well as 687-CTF and the 611-CTF proteoforms, produced by the alternative initiation of translation from the codon in the position 687 and 611, respectively[8]. These truncated forms are reported under the umbrella term p95HER2, which may include other truncated forms produced by the cleaving activity of metalloproteases, caspases, and calpains[8,9]. The p95HER2 proteoforms, present in approximately 30% of HER2+ patients, have been related to an increased aggressiveness, poor prognosis, and metastatic potential[8,10,11]. Notably, due to the absence of their extracellular domain, these proteoforms can evade therapies targeting the HER2 extracellular domain (i.e., trastuzumab). However, the p95HER2 proteoforms may still respond to combination strategies: trastuzumab paired with chemotherapy has shown efficacy, likely through chemotherapy-mediated sensitization[12]. Interestingly, HER2 levels in 611-CTF-expressing cells increased upon treatment with the chemotherapeutic drug doxorubicin[12]. The capacity of doxorubicin to induce de novo structural variants and genomic heterogeneity[13] may impact the induction of HER2 expression in p95HER2+ cells. Although extracellular domain-targeting agents are ineffective against truncated HER2 proteoforms, intracellular inhibitors like lapatinib remain active. For instance, cells expressing p95HER2 treated with lapatinib inhibited cell growth due to a reduction of the downstream phosphorylation of Akt and mitogen-activated protein kinases (MAPK)[14]. These findings and recent initiatives in proteoform definition underscore the importance of proteoform profiling in guiding therapeutic decisions in diseases, including cancer[15].

Integrating diverse data modalities has become instrumental in obtaining a complete picture of cellular states and unraveling tumor biology, since different molecular data types may result in varying degrees of biological redundancy. Protein data often shows an intermediate degree of redundancy with transcriptomic and epigenetic markers but has limited association to copy number aberrations[16]. Epigenetic markers are increasingly recognized as key determinants in tumor progression, metastasis, and tumor fate[17,18]. Among these epigenetic markers, chromatin state shifts have been observed across basal and luminal breast cancer lineages, within molecular subtypes, and between primary tumors and metastatic sites[19–22]. Epigenetic modifications frequently precede changes in protein expression, with chromatin structure predictive of coordinated RNA-protein regulatory networks[21]. Nonetheless, the correlation between RNA and protein is only intermediate[16], reinforcing the value of integrating multiple data modalities, even among moderately redundant ones, to comprehend and predict tumor behavior[16,23,24]. For this reason, in studying the role of HER2 proteoforms, we aim to explore the influence of such proteoforms on epigenetic regulation by using chromatin accessibility and protein expression as our measurement types. Although multiple methods exist for simultaneous chromatin accessibility and protein analysis, such as bulk approaches combining chromatin accessibility[25] analysis with proteomic techniques, or single-cell methods such as TEA-seq[26], DOGMA-seq[27], or NEAT-seq[28], to the best of our knowledge, a key limitation is the detection of proteoforms.

To address this gap, we introduce EpiBlot, an integrated multiomic analysis of HER2-related breast cancer model systems by combining chromatin profiling by transposase-accessible chromatin with sequencing (ATAC-seq)[25] and targeted protein expression analysis by single-cell western blotting (scWB)[29–32]. To perform ATAC-seq, we developed a plate-based method utilizing a mini-96-well plate that accommodates less than 20 µL total reaction volume and requires only 5–500 nuclei, without the need for a thermoshaker during the tagmentation step. The scWB analyzes protein and proteoform expression with single-cell resolution. One of the main advantages that lead us to choose the scWB as a counterpart to ATAC-seq is the capability of the scWB to stably archive solubilized protein targets by covalent bonding to the gels[33]. This single-

cell lysate archiving allows retrospective protein analysis. Thus, we selected our protein targets based on the differential chromatin accessibility observed in the ATAC-seq dataset. While ATAC-seq was used for target selection, the use of a single-cell technique for protein analysis explores intratumoral heterogeneity landscapes.

Using EpiBlot, we successfully profiled chromatin accessibility and protein expression in MCF7 cells transfected with different HER2 proteoforms for their multiomic profiles, revealing that HER2 611-CTF broadly impacts chromatin expression. We then analyzed how the presence of HER2 proteoforms affects the response to two different drugs: a HER2-targeted tyrosine kinase inhibitor (lapatinib) and a chemotherapeutic agent (doxorubicin). While lapatinib induced only moderate changes, doxorubicin produced a widespread effect across the chromatin landscape. Finally, we extended our analysis to clinical samples, with three patient-derived breast cancer organoids (PDOs) – two triple negative breast cancers (TNBCs) classified as HER2-low and one from normal tissue as a control – to evaluate the chromatin profiles and HER2 proteoform expression.

Results and Discussion

HER2 proteoform expression widely impacts chromatin accessibility

To understand the impact of HER2 proteoforms on chromatin accessibility, we evaluated TET-off MCF7 cell lines engineered to express distinct HER2 proteoforms, kindly provided by the Arribas lab[9]. These cell lines provide three conditions: MCF7 parental, transduced with an empty vector; MCF7 p185, containing the full-length HER2 protein (185 kDa); and MCF7 611-CTF, expressing the truncated 611-CTF HER2 fragment (110 kDa) (**Fig. 1A**). We first validated the expression of the HER2 protein (**Fig. 1B**). As expected, MCF7 parental cells presented minimal HER2 signal, consistent with null to low HER2 expression in MCF7 cells[34]. MCF7 p185 presented only the expected full-length proteoform (185 kDa). In contrast, MCF7 611-CTF presented both the full-length and the truncated proteoforms. Immunofluorescence staining confirmed HER2 localization to the cell membrane (**Supplementary Fig. 1**)

To enhance the molecular and phenotypic characterization of these HER2-expressing cell lines, we performed nuclear morphological imaging on the same sample set. Nuclear morphology can provide information about biological states such as aneuploidy, genomic instability, transcriptional dysregulation, and genetic mutations[35]. Further, nuclear morphology in cancer, including differences in nuclei that have been observed between different subtypes of breast cancer, has been shown to correlate with diagnosis[35–37]. To explore morphological changes associated with HER2 overexpression, we stained the nuclei with Hoechst 33342 to quantify nuclear area, circularity and roundness. Given that the sole variable across our conditions was HER2 proteoform expression, we aimed to determine whether the expression of these proteoforms influences nuclear architecture. As shown in **Fig. 1C,** nuclear area increased significantly ($p<0.0001$, MCF7 parental n=233, MCF7 p185 n=115, and MCF7 611-CTF n=104 nuclei) with HER2 overexpression, and this effect was further amplified in cells expressing the 611-CTF fragment. When normalized by the cytoplasm area, we observe no changes between MCF7 parental and MCF7 p185, but there is an increase in nuclear area in MCF7 611-CTF, as confirmed by the increased nuclear length ($p<0.5$). Although we observed significant differences ($p<0.5$) in circularity, length, and grey intensity of some of the nuclei, no trends were observed (**Supplementary Fig. 2**). To the best of our knowledge, the mechanistic basis of nuclear enlargement remains unclear. In breast cancer,

nuclear size, atypical features, and pleomorphism are included in standard grading systems, with higher nuclear grades correlating with worse overall prognosis[38]. In this case, we observe the largest nuclear areas in MCF7 611-CTF cells, which correspond to aggressive tumors[9].

To assess the impact of HER2 proteoforms on chromatin organization, we compared the chromatin accessibility profile across the three engineered MCF7 cell lines. To do so, we introduced a modified ATAC-seq protocol, called plateATAC-seq. The plateATAC-seq tagments ~300 nuclei, carrying all the PCR steps sequentially in that same microtiter plate microwell, eliminating the tube transfer and column cleanup post-tagmentation, minimizing sample loss, and dispensing with the thermal shaker required to keep 50,000-nucleus bulk reactions in suspension. Because all steps remain on-plate, the workflow is inherently automation-friendly, allowing microtiter plate microwells to be processed in parallel and thereby maximizing experimental scale while conserving precious nuclei (**Supplementary Fig. 3A**).

We first optimized the plateATAC-seq workflow by titrating the Mg^{2+}-chelating quench with EDTA and the amplification parameters (**Supplementary Fig. 3B**). Stopping tagmentation with 25–50 mM EDTA at 50 °C, followed by 12 PCR cycles, maximized library yield while preserving fragment integrity; the cycle number can be proportionally reduced for larger nuclear inputs. Using these conditions, we generated 43 libraries from MCF7 cells subjected to five treatment conditions. **Supplementary Fig. 3C** presents the quality of the pooled library of 43 samples with TapeStation electropherogram displaying well-resolved nucleosomal peaks: nucleosome-free (~180–200 bp), mononucleosome (~349 bp), and dinucleosome (~550 bp), confirming proper fragment sizing. In parallel, qPCR amplification curves for three serial dilutions exhibit the expected log-linear shift, further validating library integrity post-pooling. Four standard QC metrics are summarized in **Supplementary Fig. 4.** The plateATAC-seq protocol consistently achieved a median fraction of reads in peaks (FriP) of ~0.60, library complexities of $3–4 \times 10^7$ unique fragments, and mitochondrial read fractions below 0.20. Taken together, these are values that match, and in some cases exceed, those reported for conventional bulk (50,000-nucleus) or commercial single-cell ATAC-seq platforms[39] as shown in **Supplementary Fig. 4A**. Genome-browser tracks confirmed that chromatin-accessibility landscapes generated from 300-nucleus plateATAC-seq libraries recapitulate those obtained from 50,000-nucleus bulk preparations at both genome-wide and locus-specific levels (**Supplementary Fig. 4B**). Insert-size distributions retained the expected mono- and dinucleosomal periodicity (**Supplementary Fig. 4C**), and transcription-start-site metaplots showed the characteristic peak at 0 bp with symmetrical decay across ± 3 kb (**Supplementary Fig. 4D**). Together, characterization of plateATAC-seq shows that performing tagmentation, quenching, and PCR sequentially in a single 15 µL microtiter plate microwell not only preserves assay fidelity but also obviates tube transfers and column clean-ups, making the method readily automatable and ideally suited to precious or limited samples – including the PDO models profiled here.

We then profiled chromatin accessibility across our three MCF7 models: the parental line, cells expressing full-length HER2 (p185), and cells expressing the truncated 611-CTF proteoform, to identify proteoform-specific regulatory signatures. A representative locus is shown in **Fig. 1D**: accessibility tracks at the *ERBB2* (HER2) gene reveal distinct peak architectures among the three lines, illustrating the pronounced remodeling driven by the 611-CTF isoform relative to both the parental and p185 cells. Genomic feature distributions were comparable across cell lines (**Supplementary Fig. 5A**). Following peak calling from ATAC-seq data across the genome and

gene-associated regions, we performed principal component analysis (PCA), which revealed that MCF7 parental, p185, and 611-CTF cells exhibit distinct chromatin accessibility profiles. The first two components accounted for 85% and 15% of total variance, respectively (**Fig. 1E**). To further quantify these differences, we performed differential accessibility analysis using DESeq2. This analysis identified significantly differentially accessible regions (DARs) (adjusted $p < 0.05$, $|\log_2 FC| > 1$), as shown in the volcano plots (**Fig. 1F**). MCF7 parental and MCF7 p185 presented minimal differences in the differentially accessible chromatin regions, consistent with their shared expression of HER2, despite different abundance levels. The 611-CTF fragment, however, led to substantial changes in chromatin accessibility, resulting in distinctly differentially accessible chromatin regions to both MCF7 parental and MCF7 p185 cells. A comparative analysis between MCF7 611-CTF and MCF7 p185 cells revealed increased chromatin accessibility at genes involved in some key oncogenic pathways, such as the Akt pathway (*AKT1* and *HSP90AA1*) and MAPK pathway (*MAPKAPK2*, *HRAS*, and *CACNB3*, among others), as well as several PAM50 genes (*CDH3*, *BIRC5*, and *CCNE1*). *TP73*, a regulator of p53, is also highly open in MCF7 611-CTF cells[40], which could be potentially consistent with the higher aggressivity of the tumors expressing this proteoform. Conversely, several genes showed reduced accessibility in MCF7 611-CTF cells compared to the p185. These include *NFIB*, a gene responsible for the remodeling of chromatin in small cell lung cancer[41]; *KLF4*, a tumor suppressor[42]; *TRIM14*, whose downregulation inhibits cell proliferation while enhancing apoptosis[43]; or *FRK*, a kinase associated with cell proliferation, migration, and invasiveness[44].

Lapatinib has limited impact on HER2 proteoform-expressing cell lines

To evaluate the response of HER2 proteoform-expressing cells to a targeted therapy, we tested the effects of the tyrosine kinase inhibitor lapatinib. As lapatinib inhibits the phosphorylation of the intracellular tyrosine kinase domain of HER2 (**Fig. 2A**), the drug remains effective against truncated forms of HER2 such as 611-CTF[14,45]. Nonetheless, HER2 611-CTF forms homodimers maintained by disulfide bonds[46], potentially influencing downstream signaling and response to kinase inhibition.

We induced the cells via doxocycline and followed with lapatinib treatment. Morphological analysis of nuclei showed a significant increase in nuclear area in MCF7 parental and MCF7 p185 following treatment (MCF7 parental n_{DMSO}=194, n_{LAP}=156; MCF7 p185 n_{DMSO}=90, n_{LAP}=225, $P \leq 0.0001$, $P \leq 0.001$, respectively), despite the inhibition of the pathway. This tendency is maintained if the ratio between nucleus and cytoplasm is taken into consideration (**Supplementary Figure 2**). This was not the case in MCF7 611-CTF (MCF7 611-CTF n_{DMSO}=151, n_{LAP}=101, not significant), although when we evaluated the ratio, we observed a decrease in area after treatment. Interestingly, we observed that DAPI intensity was significantly increased in MCF7 611-CTF, despite no consistent size changes on the nucleus , while opposite was true for the other two cell lines. Lapatinib treatment had a modest impact on global chromatin accessibility. The number of differentially accessible regions was limited: 23 regions for MCF7 611-CTF, followed by MCF7 parental with 87 regions, and MCF7 p185, with 159. PCA revealed that PC1, which accounts for 82% of the total variance, separates samples primarily by cell line, whereas PC2 (8% variance) captures differences between treatment conditions (**Fig. 2C**). The dominant contribution of PC1 indicates that HER2 proteoform status exerts a stronger influence on chromatin accessibility than lapatinib treatment under these conditions. For instance, the *ERBB2* locus showed minimal accessibility changes following treatment across all three cell lines (**Fig. 2D**), and no strong

differences were observed based on treatment (**Fig. 2E**). The low number of differentially accessible regions suggests a limited effect of lapatinib on global chromatin remodeling. Nonetheless, a direct comparison of the treated cell lines MCF7 p185 and 611-CTF reveals widespread changes in chromatin accessibility (**Fig 2F**). This finding highlights how the expression of HER2 proteoforms can profoundly alter the cellular response to therapy. Through a gene ontology enrichment analysis, we observe MCF7 611-CTF-specific pathways include *ERBB* signaling, *Wnt* signaling, and ERK1/2 cascade regulation, suggesting a strong enrichment of HER2-related pathways in MCF7 611-CTF under lapatinib treatment (**Fig. 2G-H**). In contrast, MCF7 p185-specific pathways involve MAPK activity and Ras protein signaling, as previously reported in HER2+ cells[47,48], and TOR signaling, a pathway involved in lapatinib resistance[49,50]. These differences in downstream signaling responses to lapatinib suggest distinct effects of the two HER2 proteoforms. Shared pathways include MAPK cascade regulation and Wnt signaling, highlighting common chromatin accessibility changes between the two cell lines.

Based on the results of the plateATAC-seq analyses, we scrutinized protein targets (**Fig. 2I**) in individual cells by scWB. The use of scWB offers several additional advantages: sample material requirements are notably less than a conventional WB, and single-cell resolution reports heterogeneity of protein expression among a cell population. As control proteins, we included HER2 and β-tubulin. In addition, and based on the plateATAC-seq results, we selected ULK1, a protein that induces autophagy[51], and TFAP2C, a regulator of estrogen receptor expression in breast cancer[52]. Only two proteins were selected given the limited number of changes observed. MCF7 parental shows a decrease in expression of ULK1, which corresponds well to the decrease in open regions for the *ULK1* gene (**Fig. 2I** and **Supplementary Fig. 6-7**). Although no changes were observed in the differential accessibility in MCF7 p185 and 611-CTF, we did observe a significant increase in ULK1 expression in both cell lines. Similarly, an increase was observed in TFAP2C abundance in MCF7 p185, although the TFAP2 locus closed after treatment.

Doxorubicin induces distinct chromatin accessibility profiles in HER2 proteoform-expressing cells

We then sought to evaluate how the HER2-transfected cells respond to the chemotherapeutic drug doxorubicin. Doxorubicin is a broadly-used anthracycline that functions by sequestering DNA topoisomerase II to create DNA double-strand breaking points[53,54], leading to apoptosis of the cells (**Figure 3A**). In addition to inducing DNA damage, doxorubicin evicts histones from specific genomic regions[55], and alters nucleosomal occupancy levels on cancer related genes, potentially promoting genomic instability[13]. Given the impact that doxorubicin has on chromatin, we decided that this drug was a good model for investigating chromatin accessibility changes produced by HER2 and potentially its proteoforms.

We first induced HER2 expression in the HER2-proteoform transfected cell lines through the incorporation of doxocycline to the culture medium, and then we treated the cells with 1 μM of doxorubicin for 48 h. We then analyzed the morphology of the nuclei pre- and post-treatment (**Fig. 3B, Supplementary Fig. 2B**). Both MCF7 parental and MCF7 p185 presented a significant nuclei enlargement following doxorubicin treatment (MCF7 parental n_{DMSO}=233, n_{DOXO}=75; MCF7 p185 n_{DMSO}=115, n_{DOXO}=17; MCF7 611-CTF n_{DMSO}=104, n_{DOXO}=28, $P \leq 0.0001$, $P \leq 0.001$, and not significant, respectively), while MCF7 611-CTF remained similar. If we observe the ratio between

nuclear and cytoplasmic area, all of the conditions showed an increase after treatment, indicating that the nucleus increased in area more than the cytoplasm.

To determine the effects of doxorubicin on chromatin accessibility, we performed plateATAC-seq on treated and untreated samples from each cell line. To assess whether doxorubicin-induced changes were biologically stochastic, we performed plateATAC-seq on three biological replicates per condition of the treated cells and performed PCA (**Figure 3C**). Both in treated and untreated conditions, the three replicates cluster together, indicating similarity in the chromatin remodeling profiles. Treated and untreated conditions were clearly separated for all the three conditions, with MCF7 611-CTF presenting the greatest separation. In contrast, MCF7 parental and MCF7 p185 were clustered more closely together. An example of the changes in chromatin accessibility is shown in **Figure 3D**, where the *ERBB2* gene shows decreased accessibility following treatment across all conditions. The impact of doxorubicin treatment on chromatin accessibility on selected genes is visualized in **Figure 3E**. *CDK6* exhibits increased accessibility only in the doxorubicin-treated condition, while *PIK3R2* is selectively closed in MCF7 611-CTF doxorubicin-treated samples but remains accessible in other cell lines and conditions. Differential accessibility analysis reveals that doxorubicin treatment has an extensive impact in chromatin accessibility (**Figure 3F)**. MCF7 611-CTF exhibits the highest number of differentially accessible regions (~64,768), followed by MCF7 p185 (~48,785) and MCF7 parental (~34,017), suggesting a stronger chromatin remodeling response in MCF7 611-CTF. Differentially accessible regions (FDR-adjusted p-value < 0.001) with significant chromatin accessibility changes include *CCND1*, which is downregulated (more closed chromatin) in doxorubicin-treated MCF7 611-CTF, suggesting suppression of cell-cycle regulation. *GATA3* shows closed accessibility in doxorubicin-treated MCF7 p185, potentially indicating downregulated transcription factor activity. *AZIN1-AS1* exhibits greater accessibility in doxorubicin-treated MCF7 parental and MCF7 p185 cells, while remaining unchanged in MCF7 611-CTF (**Fig. 3F**). The gene ontology enrichment pathway analysis shows that MCF7 611-CTF has a strong enrichment in pathways related to epithelial-mesenchymal transition, *ERBB2* signaling, and cell adhesion, whereas doxocyclin-treated MCF7 p185 is enriched in pathways related to RNA splicing, histone modification, and *Wnt* signaling (**Figure 3G**). Shared pathways include *ERBB2* signaling, *MAPK* cascade regulation, and DNA-binding transcription factor activity, suggesting common and distinct chromatin accessibility responses to doxorubicin in these HER2 proteoforms.

Following the plateATAC-seq analysis, we tested a selection of protein markers by scWB. Here, we again included HER2 and β-tubulin as controls. Additional targets included GATA3, a transcription factor implicated in the luminal differentiation of breast epithelium[56]; EGR1, a protein with both tumor-suppressor and tumor-promoter activities[57]; BCAS3, associated with chemoresistance through a p53-mediated mechanism[58]; and PPP1R13L, implicated in tumorigenesis[59] (**Fig. 3H-I, Supplementary Fig. 7A, and Supplementary Fig. 8A**). PCA of single-cell protein expression profiles shows that treated and untreated cells form partially overlapping clusters, indicating that the protein-level differences are not completely distinct (**Supplementary Fig. 8B**). The partial separation is a product of multiple proteins showing significantly different expression between the treated and non-treated expression ($P<0.05$, ANOVA test), especially in the case of MCF7 p185 (**Supplementary Fig. 8C**). Despite changes in both chromatin accessibility and protein abundance, we observed a wide dynamic range of protein expression across individual cells, a hallmark of a heterogeneous response to doxorubicin (**Fig. 3H**).

Identification of subpopulations and divergent accessibility patterns in tumor organoids

To test the compatibility of our approach with clinical samples, we used patient-derived organoids. Organoids are frequently used tumor models, capable of preserving the cellular heterogeneity and overall complexity of the tumors from which they are derived[60], making them more physiologically relevant systems. In this study, we examined a cohort of 2 breast cancer PDOs and one normal breast PDO, derived from tumor-adjacent non-tumorous normal breast tissue for comparison (**Fig. 4A**). We specifically selected TNBC organoids to investigate the behavior of HER2-low phenotypes in a relevant context, given the emerging significance of HER2 expression gradients in TNBC. The TNBC organoids were confirmed to be HER2 low by immunofluorescence (**Supplementary Fig. 9**).

Dissociated organoids were divided in two fractions, one submitted for plateATAC-seq and the other reserved for scWB. Technical replicates of TNBC-1 and TNBC-2 clustered together (**Fig. 4B**), and all organoids were distinct from one another. The selected loci in **Figure 4C** show that TNBC-1 exhibits strong chromatin accessibility upstream of *BRCA2* and *STAT3*, while TNBC-2 has the most open chromatin in the upstream region. At *CASC11*, TNBC-2 displays the highest accessibility, whereas Normal and TNBC-1 shows a closed pattern. In the *TP53-WRAP53* region, TNBC-1 exhibits the strongest chromatin accessibility, potentially reflecting an altered regulatory state in Grade 3 compared to Grade 2 (TNBC-2) and normal tissue. Compared to Normal PDOs (due to the limited number of cells only one replicate was analyzed), TNBC organoids have fewer accessible promoter regions (≤1kb) and more distal intergenic regions, suggesting a shift toward noncoding regulatory elements in TNBC (**Fig. Supplementary 5B**). **Figure 4D** shows that TNBC-2 exhibits an opposite accessibility pattern compared to both normal controls and TNBC-1, suggesting a distinct chromatin remodeling profile in this TNBC subtype. Notably, genes involved in cancer-related pathways, including *MTOR*, *JUN*, *STAT3*, *MYC*, *TP53*, and *CTNNB1*, show differential chromatin accessibility, indicating potential regulatory divergence in TNBC-2 compared to other TNBC models. Both cancer organoids present a downregulation of *ERBB2* compared to the Normal organoid, despite showing an enrichment the MAPK pathway (gene ratio 0.04) in TNBC-1, and PI3K-Akt and MAPK in TNBC-2 (gene ratio 0.05 and 0.045) (**Supplementary Fig. 10**). Both TNBC-1 and TNBC-2 exhibit distinct chromatin accessibility profiles compared to Normal (**Fig. 4E**). TNBC-1 shows more closed chromatin regions relative to Normal, suggesting widespread chromatin compaction, while TNBC-2 exhibits a more balanced mix of open and closed regions, indicating differential chromatin remodeling between TNBC organoid models.

We evaluated the protein expression of GATA3, ULK1, EGR1, PPP1R13L, HER2, and β-tubulin across the three sequenced organoids, based on the previous selection of markers (**Supplementary 11A**). We did not observe a distinctive clustering of either of the organoids based on protein markers (**Supplementary Fig. 11B**). Interestingly, we detected a small cell subpopulation (n=3, i.e., 0.3% of examined cells) in TNBC-1, which expressed the truncated HER2 proteoform (**Supplementary Fig. 11C**). The number of truncated cells could be higher, since we observed several scWB bands with a weak signal in the molecular weight compatible with truncated HER2 (n=26, **Supplementary Fig. 11D**). However, we discounted these weak bands from the analysis as the signal was below the quantification limit. The reduced size of the observed subpopulation could be caused by inadvertent bias in sampling into the two aliquots required for the two different

analyses, the low levels of expression of the truncated HER2 proteoforms, or the reduced size of the subpopulation. Additionally, we observed that the expression of HER2 in both TNBC organoids was significantly higher ($P<0.05$) than in the Normal tissue, despite presenting a decreased accessibility in the locus, possibly caused by changes in the accessibility of the enhancer region of *ERBB2* (**Supplementary Fig. 10C and 11E**).

Finally, we examined the correlation between protein and chromatin accessibility by comparing the Log2 fold-change for each marker (**Fig. 4F**). In both tumorous organoids, EGR1 expression is elevated, while two main peaks exist for the chromatin accessibility, one increasing 1-fold and the other decreasing 3-fold. ULK1 shows an opposite tendency for TNBC-1 and TNBC-2, with TNBC-2 increasing the expression of this protein

Discussion

In this study, we evaluated the impact of HER2 abundance and proteoform expression on chromatin accessibility using a new pooled-cell assay, called EpiBlot, which combines plateATAC-seq and a single-cell resolution protein target assay, scWB. PlateATAC-seq profiles chromatin accessibility with limited numbers of starting nuclei, while scWB archives cytoplasmic proteins for a subsequent targeted analysis on the same cell sample, mitigating batch effects. Our findings demonstrate that HER2 proteoforms exert a potent influence on cellular regulation. As an upstream receptor tyrosine kinase, HER2 plays a pivotal role in signal transduction, and variations in its expression or activity have the potential to determine cell fate. Naïve MCF7 cells are generally classified as HER2 0 or +1 ref.[61]. Overexpression of full-length HER2 resulted in relatively modest alterations to the chromatin accessibility landscape, with only 7 differentially accessible genes. In contrast, expression of a truncated, constitutively active HER2 proteoform produced a substantial shift in chromatin architecture, yielding between 100 and 2,400 unique differentially accessible regions when compared to MCF7 parental and p185. This underscores the profound regulatory impact of specific proteoform identity beyond overall HER2 expression levels.

As anticipated for a targeted therapy, lapatinib had a more limited effect on chromatin accessibility. Interestingly, MCF7 611-CTF cells exhibited fewer differentially accessible genes. The clinical significance of p95HER2 expression in lapatinib-treated patients remains unclear, with some reports associating it with longer survival[62] and others finding no significant impact[63]. These discrepancies likely reflect differences in study design, treatment regimens, and patient populations.

Cell-line identity emerged as a key determinant in response to chemotherapeutic treatment. Doxorubicin, a DNA intercalating agent, induced widespread changes in chromatin accessibility across all cell lines. These effects are likely attributable to the drug's known mechanism of drug action, which involves chromatin intercalation and disruption of DNA topology. The potential impact of HER2 amplification on anthracycline efficacy has been debated, with some studies reporting enhanced therapeutic responses in HER2+ tumors[64–67] and highlighting sensitization of p95HER2/611-CTF-expressing xenografts to trastuzumab[12]. However, a recent meta-analysis has failed to establish a consistent link between anthracycline administration and complete clinical response in HER2+ patients[68].

We identified significant changes in nuclear morphology, specifically nuclear area, associated with both HER2 proteoform expression and drug treatment. While nuclear area is influenced by multiple factors, including chromatin compaction, mechanical tension, and osmotic pressure, evidence argues against a direct correlation with chromatin condensation alone[69]. Following doxorubicin treatment, we observed a downregulation of *LMNA* and *ACTB* across all cell lines, which may contribute to increased nuclear drug uptake and a consequent increase in nuclear size[70]. A similar, though less pronounced, enlargement was observed after lapatinib treatment. Although specific studies on nuclear size changes induced by lapatinib are limited, it is plausible that shared mechanisms involving cytoskeletal or nuclear envelope alterations may contribute to a nuclear enlargement.

As protein expression reflects downstream biological states, this expression is generally expected to correlate with upstream transcriptional and epigenetic regulation. However, previous studies have shown only moderate correlations between protein levels, RNA abundance, and chromatin accessibility[16,21]. Our results align with this pattern, with the observed variance exacerbated by single-cell heterogeneity. Differential chromatin accessibility did not always translate into corresponding protein changes. This may be due to additional layers of epigenetic regulation, lack of functional relevance of the epigenetic changes, or differences in protein synthesis and degradation dynamics[71]. Future studies may consider temporally resolved measurements of chromatin accessibility and protein levels to delineate the dynamics of proteomic responses following chromatin remodeling, especially at the single cell level.

In our analysis of the PDOs, we observed a predominance of closed chromatin regions in tumor samples relative to the normal control (open vs closed: TNBC-1 35k vs 47k, and TNBC-2 32k vs 44k). This is consistent with findings in other disease states where global chromatin compaction was observed, such as macular degeneration[72] and systemic sclerosis[73]. These findings may suggest that the repression of regulatory elements may be a feature of TNBC epigenomes. Notably, despite the overall decrease in chromatin accessibility at the *ERBB2* locus, both TNBC organoids exhibited elevated HER2 protein levels, suggesting that post-transcriptional regulation or enhancer-driven expression may contribute to HER2 upregulation in these tumors. These findings highlight that, while it may appear that there is epigenetic silencing of the *ERBB2* gene, alternative regulatory mechanisms are inducing HER2 expression. This protein upregulation may facilitate the uptake of HER2-directed drugs into the cancer cells.

Intratumor heterogeneity can be captured in PDOs[74], and we could capture such heterogeneity in TNBC-1, which presents a small subpopulation of cells expressing p95HER2. The presence of such heterogeneity in HER2 proteoform expression highlights the importance of multi-modal single-cell analysis capable of simultaneously assessing proteoform expression and chromatin accessibility, as the detected subpopulation of cells may be expressing a distinct chromatin accessibility pattern. The detection of HER2 proteoforms in a TNBC-classified organoid suggests the need of use of personalized treatments adequate to the development of tumor heterogeneity of each patient. The relevance of understanding intra-tumor heterogeneity in TNBCs has been widely explored, showing correlation to metastasis[75]. The ability to detect such rare subclones could be pivotal for stratifying patients for therapy or identifying resistance mechanisms. However, higher-throughput, integrated single-cell technologies that can simultaneously profile chromatin and proteoforms will be essential to fully capture tumor complexity. For clinical applications, such

systems would benefit of the examination of nuclear characteristics as samples derived from patients may contain fibroblasts and immune cells among tumor cells.

Together, our study reveals that HER2 proteoform diversity alters chromatin organization and modulates drug response, with truncated forms exerting more profound effects than full-length HER2.

Limitations of this study

A limitation of the technological aspect in plateATAC-seq is that, while the study is performed on a scant number of cells (300-500 cells), the initial concentration of nuclei required is high to allow the visualization of the cell pellet. Similarly, scWB presents constraints in protein analysis, with target multiplexing requiring multiple rounds of stripping and probing to analyze >3 protein targets, a process that can alter epitope availability[33]. Furthermore, while the single-cell resolution of a scWB is an advantage to understand tumor heterogeneity, reliable detection is restricted to the top half of the mammalian proteome[29].

From the biological perspective, while the use of transfected cell lines is standard in evaluating the function of a given protein, cell-line models often involve non-physiological expression levels and lack of regulatory elements present in wild-type cells[76]. Conclusions require validation and results from drug perturbation studies are not directly translatable to clinical practice. Additionally, our study considered a pilot set of PDOs. Further evaluation of resistant and sensitive PDOs will be required to determine which chromatin accessibility and proteomic changes impact response.

Key resources table

REAGENT OR RESOURCE	SOURCE	IDENTIFIER
Antibodies		
anti-HER2	abcam	ab16901 [discontinued], ab134182 (**Supplementary Fig. 12**)
Anti-HER2-AF488	Abcam	ab275994
anti-β-tubulin	abcam	ab6046
anti-TFAP2C	abcam	ab134182
anti-ULK1	ThermoFisher	8054S
anti-GATA3	ThermoFisher	14-9966-82
anti-PPP1R13L	ThermoFisher	PA5-59491
anti-BCAS3	abcam	ab71162
anti-EGR1	ThermoFisher	MA5-15008
Experimental models: cell lines		
TET-off MCF7 cells	Arribas lab, Vall d'Hebron (ref)	N/A
SKBR3	UC Berkeley Cell Culture Facility	N/A

MDA-MB-231	UC Berkeley Cell Culture Facility	N/A
Cell culture		
DMEM/F12 (Gibco)	Thermo Fisher	10565018
FBS	Gemini Bio	S11150
Geneticin (G418) (Gibco)	Thermo Fisher	10131035
Doxocycline	Takara Bio	631311
PBS (Gibco)	Thermo Fisher	10010023
Organoid culture		
Cultrex Basement Membrane Extract (BME) type 2	BioTechne	3532-010-02
DMEM/F12	Fisher Scientific	BW12-719F
Primocin	InvivoGen	ant-pm-05
GlutaMax	Thermo Fisher	35-050-061
Penicillin/Stroptomycin	Thermo Fisher	15140122
HEPES	Thermo Fisher	15-630-080
B27	Gibco	17504044
Nicotinamide	Sigma-Aldrich	N0636
N-acetylcysteine	Sigma-Aldrich	A0737
Hydrocortisone	Sigma-Aldrich	H0888
β-estradiol	Sigma-Aldrich	E4389
forskolin	Sigma-Aldrich	F6886
Y-27632	abcam	ab143784
heregulin β1	Peprotech	100-03
FGF-7	Peprotech	100-19
FGF-10,	Peprotech	100-26
A83-01	Sigma-Aldrich	SML0788
EGF	Peprotech	AF-100-15
SB202190	Sigma-Aldrich	S7067,
TrypLE Express	Gibco	12604013
DPBS	Gibco	14190144
FBS	Cytiva	SH30910.03
Chemicals		
Hoechst 33342	Invitrogen	H1399
Doxorubicin (hydrochloride)	Thomas Scientific	C819Z82
Lapatinib	Sigma-Adrich	SIAL-CDS022971-25MG
DMSO	Cell Signaling Technology	12611S
Phalloidin-rhodamine	Invitrogen	R415
16% Formaldehyde	ThermoFisher	28908
Triton-X100	Sigma-Aldrich	SIAL-X100-100ML
Tris-Glycine	Sigma-Aldrich	93321-1L
Sodium dodecacylsulfate	Sigma-Aldrich	SIAL-L3771-1KG

Sodium deoxycolate	Sigma-Aldrich	30970
acrylamide:bis-acrylamide (29:1)	Sigma-Aldrich	A3574
BP-APMA (BPMA)	Raybow Pharmaceutical	Custom synthesis
Ammonium persulfate	Sigma-Aldrich	A3678-25G
Tetramethylethylenediamine	Sigma-Aldrich	T9281-25ML
double cytology funnel	Fisher Scientific	10-356
DAPI	Invitrogen	P36931
Digitonin	Promega	G9441
Critical commercial assays		
Tagmentation buffer and enzyme	Illumina	20034197
KAPA Library Quantification Kit	Roche	07960140001
NEBNext® High-Fidelity 2× PCR Master Mix,	NEB	M0541S
Materials & Instruments		
Mini 96-well plate	Kubo Biotech	http://www.kubotechnology.com/
qPCR instrument q225	Kubo Biotech	http://www.kubotechnology.com/
Software and algorithms		
Fiji v1.54d	Schindelin et al.	https://imagej.net/software/fiji/
GraphPad Prism	GraphPad	https://www.graphpad.com/scientific-software/prism/
Python script for image analysis	This paper	https://github.com/herrlabucb/segmentation_scWB

Experimental model

Transfected MCF7 cells

Transfected MCF7 cell lines were kindly provided by the Arribas lab, with the cells reported and characterized in ref.[9]. MCF7 cells were cultured in DMEM/F-12, Glutamax supplemented with 10% FBS, 0.2 mg/mL Geneticin and 1 µg/mL doxycycline at 37°C, 5% CO_2. Media was exchanged every 48 h to avoid activation of the vector. MCF7 were maintained by dissociation into single cells at 70-80% confluency with Trypsin-EDTA 0.25% and seeded at a dilution of 1:10 in media. For expression of the TET-off vector, the cells were cultured in media without doxycycline for 48 h.

For the drug treatment, cells were cultured in doxycycline free media for 48 h. After, 1 µM of doxorubicin or 10 µM of lapatinib were deposited in the corresponding wells of the 96-well plate. For the controls, a volume of DMSO equivalent to that of doxorubicin or lapatinib in the media was added to the cells to account for the toxicity of the DMSO, the initial diluent of these drugs.

To reduce the impact of batch variation, all samples, including all treated cells with doxorubicin and lapatinib, were processed in parallel.

Organoid culture

PDOs from the Rosenbluth lab organoid biobank were cultured as described previously[60,74,77]. **Supplementary Table 1** catalogues the PDOs scrutinized here. Briefly, PDOs were embedded in Cultrex Basement Membrane Extract (BME) type 2 and plated in preheated (37°C) 24-well non-cell treated plates. TNBC PDOs were kept in type 1 organoid medium, while normal PDOs were kept in type 2 organoid medium. Organoid medium is composed of Advanced DMEM/F12 with 50 µg/ml Primocin, 1x GlutaMax, 100 units/ml Penicillin/Stroptomycin, 10 mM HEPES, 20% Wnt3a conditioned medium[77] (H. Clevers lab, Hubrecht Institute, type 2 only), 10% R-spondin 1 conditioned medium[77] (C. Kuo lab, Stanford University), 10% Noggin conditioned medium[77] (H. Clevers lab, Hubrecht Institute), 1x B27, 10 µM Nicotinamide, 1.25 mM N-acetylcysteine, 500 ng/ml Hydrocortisone (type 2 medium only), 100 nM β-estradiol (type 2 medium only), 10 µM forskolin (type 2 medium only), 5 µM Y-27632, 5 µM heregulin β1, 5 µM FGF-7 (type 1 medium only), 20 ng/ml FGF-10 (Peprotech, 100-26), 500 nM A83-01, 5 ng/ml EGF, and 1 µM SB202190 (type 1 medium only). To obtain single cells for analysis, organoid domes were digested for 10 min with TrypLE Express at 37°C followed by three washes with Advanced DMEM/F12 with 50 µg/ml Primocin, 1x GlutaMax, 100 units/ml Penicillin/Streptomycin, and 10 mM HEPES. Single cells were harvested in DPBS with 5% FBS and kept on ice until analysis.

For the tests, Normal had 1 replicate, TNBC-1 had 2 replicates, and TNBC-3 had 3 replicates.

Immunofluorescent staining of cell lines

Coverslips were placed at the bottom of a sterile 12-well plate and sterilized by washing in 70% ethanol 3x for 5 min. A fourth wash was performed with 100% ethanol for 5 min and the coverslips were dried inside the hood. A solution of poly-lysine was prepared by diluting 5 mg of poly-lysine in 50 mL of sterile water. The coverslips were coated with poly-lysine by submerging in 0.5 mL of the poly-lysine solution for 5 min. After, the coverslips were rinsed with water and dried for 2 h.

Cells were trypsinized and cultured on the coverslip inside a 12-well plate, following the culturing conditions described in "Transfected MCF7 cells". After, the media was removed and cells were washed in PBS. The PBS was substituted by 4% paraformaldehyde diluted in PBS for 20 min. The coverslips were washed 2x with PBS and the cells were permeabilized with 0.25% Triton X-100 in PBS for 5 min. Cells were then washed 2x in PBS.

The next step was the primary antibody staining. A solution of 1% BSA in PBS solution with 2.5 µg/mL of anti-HER2 antibody, 1 µg/mL of Hoescht, and 0.033 µM of phalloidin-rhodamine was prepared. A volume of 125 µL of the antibody solution was added to each coverslip and then incubated at 37°C for 3 h in a humidity chamber. The coverslips were then washed 5 times for 3 min in 0.1% Tween-20 in PBS on a rotator. For the secondary antibody staining, a solution containing anti-mouse-488 antibody at 2.5 µg/mL in 1% BSA with PBS was prepared and the coverslips were incubated in 125 µL of antibody solution for 1 h at 37°C in a humidity chamber. The coverslips were then washed in 0.1% Tween-20 in PBS 5x for 3 min. A drop of mounting media was deposited on the coverslip and a glass slide was sealed on top. The slide was dried overnight and sealed with nail polish before imaging using the Agilent/Biotek LionHeart system.

Immunofluorescent staining of PDOs
PDOs were digested to single cells as described above and fixed in 2% paraformaldehyde for 15 min. Cells were washed 3x with PBS and loaded onto a double cytology funnel. Cells were spun onto microscope slides by centrifugation at 800 rpm for 3 min using a Thermo Scientific Cytospin 4 Centrifuge. Slides were then air-dried for 1 h followed by permeabilization with cold 0.5% Triton-X in PBS for 10 min at 4 °C. Subsequently, slides were washed 3x with PBS and then blocked with 10% goat serum in TBS-T for 1 h at room temperature. Slides were incubated overnight with an anti-HER2 antibody conjugated to AF488 (1:200) diluted in 1% goat serum in TBS-T. After 3x washes with TBS-T, slides were mounted with ProLong™ Gold Antifade Mountant with DAPI and imaged using an ECHO Revolve Fluorescent Microscope.

Isolation of nuclei
ATAC-RSB (10 mM Tris-HCl pH 7.4, 10 mM NaCl, 3 mM $MgCl_2$) was prepared from stock reagents and supplemented to make lysis buffer (0.1 % IGEPAL CA-630, 0.1 % Tween-20, 0.01 % digitonin) or wash buffer (0.1 % Tween-20). One million viable cells were pelleted (500 × g, 5 min, 4 °C), washed once in ice-cold PBS, and lysed in 300 µL lysis buffer (10 gentle mixes, 5 min on ice; 4 min for organoids). Lysis was quenched with 1 mL wash buffer, nuclei were pelleted 2x (hinge in/out, 500 × g, 3 min, 4 °C), and resuspended in 250 µL wash buffer with a wide-bore tip. Nuclei counts were determined on a Countess (Trypan Blue). Aliquots of 100,000 nuclei were diluted, re-pelleted, and adjusted to the desired concentration.

Plate-based tagmentation and library preparation

plateATAC-seq begins by tagmenting ~300 nuclei in a single 15 µL microtiter plate microwell. A tagmentation mix was prepared using 1X Tagmentation buffer (Illumina Inc), 0.1% Tween 20, and 0.01% digitonin (Promega). TDE1 tagmentation enzyme (Tn5, Illumina Inc) was added to the mix at a ratio of 1:15. Then, 1.5 µL of nuclei (~300 nuclei) were aliquoted into a mini 96-well plate (Kubo Biotech), followed by the addition of 2.5 µL of the tagmentation mix. The plate was sealed with PCR tape and incubated for 30 minutes at 37°C in a qPCR instrument (q225, Kubo Biotech).

Instead of stopping the reaction with an elution-and-column cleanup, as in conventional bulk ATAC-seq[25], we quench Tn5 by adding EDTA to chelate $MgCl_2$ directly in the micro-titer plate microwell. To terminate the tagmentation reaction, 2 µL of stop buffer (0.025 M EDTA, 0.015 M Tris-HCl, pH 8.0) was added to each microtiter plate microwell, and the mixture was incubated for 30 minutes at 50°C. For library amplification, 9 uL of PCR mix containing 1X NEBNext® High-Fidelity 2X PCR Master Mix, 1.25 µM i5 primer, and 1.25 µM i7 primer was added to each microtiter plate microwell. The amplification protocol was as follows: 72°C for 5 min and 98°C for 30 s; followed by 10 cycles of 98°C for 10 s, 63°C for 30 s, and 72°C for 60 s. PCR products were purified using the Zymo DNA Clean and Concentrator-5 kit. DNA concentration was quantified using a Qubit fluorometer, and the nucleosomal pattern was assessed using an Agilent TapeStation with D1000 tape and reagents.

Libraries from all MCF7 cell lines or organoids were quantified with the KAPA Library Quantification Kit (Roche), pooled equimolarly to 1.07 ng μL^{-1} for cell lines and 1.70 ng/uL for organoids, and quality-checked by TapeStation and Qubit. The pooled library containing the cell lines was sequenced on two NovaSeq 6000 S2 lanes (~3 billion clusters total) with 2 × 75 bp reads while the organoids pooled library was sequenced on NextSeq 2000 P2 (400 million clusters).

Soft lithography for fabrication of single-cell western blot microdevices
Soft lithography for scWB molds were fabricated as previously reported[29]. A 40-µm layer of SU-8 3050 was spun over a silicon wafer for 10 s at 500 rpm with an acceleration of 100 rpm, and then for 30 s at 4000 rpm with an acceleration of 300 rpm. The wafer with the SU-8 later was soft baked for 2 min at 65°C, 15 min at 95°C and then 3 min at 65°C. The wafer was then exposed to a UV dose of 385 mJ/cm2 and baked post-exposure for 1 min 65°C, 5 min at 95°C and then 1 min at 65°C. To remove excess of SU-8, the wafer was developed for 5 min on a shaker and then hard baked at 200°C for 20 min.

Single-cell western blotting
The scWB was performed as previously described[29,78]. Briefly, gels were fabricated mixing 7% acrylamide:bis-acrylamide, 3 mM BPMA, 0.08% ammonium persulfate, and 0.08% tetramethylethylenediamine. The precursor solution was introduced to the gap between a patterned wafer and a silanized glass slide until the gel was polymerized after 15 min. The gel was detached from the wafer and washed in PBS for 1h. The gel was then dried under a nitrogen stream to increase the probability of deposition of a cell in each microwell.

For cell lines, 250 µL of 1 million/mL of strained cells were deposited on each gel. The dimensions of the gel correspond to half of a microscope glass slide. In the case of organoids, in all cases the concentration of cells was below 1 million/mL and thus the available concentration was deposited on the gel in 250 µL. After 10 min, the excess cells were carefully removed by tilting the slide and washing it with PBS. The gels were deposited in a custom 3D printed chamber that contained two platinum electrodes separated by 6 cm. The cells were lysed by applying RIPA buffer (1% w/v SDS, 0.5% w/v sodium deoxycholate, 0.1% v/v Triton X-100, and 0.5× of Tris-glycine) for 30 s and then energizing an electrical field of 40 V/cm was applied for 30 s to perform electrophoresis. The gels were photoactivated (45 s) to covalently immobilize proteins with the BPMA in the polyacrylamide gel. The gel was then deposited in a volume of 1× TBS + 0.1% Tween-20 (TBST) for >1 h. The gel was then incubated in 40 µL of primary antibody for 1 h (100 µg/mL for β-tubulin, TFAP2C, GATA3, SULF2, and HER2, 42.5 µg/mL for BCAS3, 20 µg/mL for PPP1R13L, 10 µg/mL for ULK1, 9 µg/mL for EGR1), washed in TBST for 45 min with one wash exchange after 20 min, and incubated with the secondary antibody for 1 h (100 µg/mL). The sample was washed in TBST for 45 min with one wash exchange, and then rinsed in water to remove salts. The gel was dried under a nitrogen stream and imaged using Genepix Microarray Scanner (Genepix 4300A, Molecular Devices), with a resolution of 5 µm.

Data analysis
All ATAC-seq downstream data analyses were performed in R 4.2.2. Upstream data analyses including peak calling and per-sample quantification (featureCounts) were produced by the nf-core/atacseq v2.0 pipeline, then imported as a DESeqDataSet. Sample metadata were parsed from file names to create a design ~group, and differential accessibility was assessed with DESeq2 (Wald test, BH < 0.05). Peaks were annotated to nearest genes (±3 kb TSS) with ChIPseeker / TxDb.Hsapiens.UCSC.hg38.knownGene, functional enrichment was performed with clusterProfiler::enrichGO, and results were visualized with ggplot2, pheatmap, and EnhancedVolcano.

scWB protein data analyses were performed usinf a custom the Python algorithm workflow adapted from ref.[79], using numpy, pandas, tkinter, and pillow (**Supplementary Fig. 13**). All

analyses of scWB were performed on raw image data. For improved visualization, figures showing the scWB protein bands have been grayscale inverted and adjusted for contrast.

Nuclear characteristics (circularity, length and area) were quantified using MicrobeJ[80]. The segmentation of the nucleus and the cytoplasm for all conditions was performed using UNSEG[81].

Schemes were created with BioRender.

Statistical tests
Bar graphs were compared using two-way ANOVA followed by Tuckey's multiple comparison tests. Nuclear dimensions were compared using the Mann–Whitney U test to account for skewed data.

Acknowledgements

A.E.H. and J.M.R. acknowledge financial support from the Investigator Program of the Chan Zuckerberg Biohub San Francisco. A.E.H. acknowledges support from the US National Institutes of Health (NIH R01CA20301). J.M.R. thanks the Dana-Farber Cancer Institute Breast Biospecimen Users Committee, DF/HCC Breast SPORE 1P50CA168504, NIH 5R01CA281361, and METAvivor. A.F.K. acknowledges support from the Swiss National Science Foundation (SNSF) Postdoc Mobility fellowship (P500PN_214236). Photolithography was performed in the QB3 Biomolecular Nanotechnology Center at UC Berkeley, imaging was performed at the Cell & Tissue Analysis Facility at UC Berkeley, and the sequencing at the Genomics Platform at the San Francisco CZ Biohub. We thank Dr. Alison Su and Dr. Angelika Feldmann for helpful discussions. We thank Joaquin Arribas, PhD and his lab for providing the MCF7 transfected cells.

The content is solely the responsibility of the authors and does not necessarily represent the official views of the National Institutes of Health/NCI.

Declaration of generative AI and AI-assisted technologies in the writing process.

During the preparation of this work the authors used ChatGPT in order to improve readability. After using this tool/service, the authors reviewed and edited the content as needed and took full responsibility for the content of the published article.

References

1. Bray, F., Laversanne, M., Sung, H., Ferlay, J., Siegel, R.L., Soerjomataram, I., and Jemal, A. (2024). Global cancer statistics 2022: GLOBOCAN estimates of incidence and mortality worldwide for 36 cancers in 185 countries. CA: A Cancer Journal for Clinicians *74*, 229–263. https://doi.org/10.3322/caac.21834.

2. American Cancer Society (2024). Breast Cancer Facts & Figures 2024-2025 (Atlanta: American Cancer Society).

3. Schlam, I., and Swain, S.M. (2021). HER2-positive breast cancer and tyrosine kinase inhibitors: the time is now. npj Breast Cancer *7*, 56. https://doi.org/10.1038/s41523-021-00265-1.

4. Premji, S.K., and O'Sullivan, C.C. (2024). Standard-of-Care Treatment for HER2+ Metastatic Breast Cancer and Emerging Therapeutic Options. Breast Cancer (Auckl) *18*, 11782234241234418. https://doi.org/10.1177/11782234241234418.

5. Modi, S., Jacot, W., Yamashita, T., Sohn, J., Vidal, M., Tokunaga, E., Tsurutani, J., Ueno, N.T., Prat, A., Chae, Y.S., et al. (2022). Trastuzumab Deruxtecan in Previously Treated HER2-Low Advanced Breast Cancer. New England Journal of Medicine *387*, 9–20. https://doi.org/10.1056/NEJMoa2203690.

6. Corti, C., Giugliano, F., Nicolò, E., Tarantino, P., Criscitiello, C., and Curigliano, G. (2023). HER2-Low Breast Cancer: a New Subtype? Curr. Treat. Options in Oncol. *24*, 468–478. https://doi.org/10.1007/s11864-023-01068-1.

7. Hu, X., Yang, P., Chen, S., Wei, G., Yuan, L., Yang, Z., Gong, L., He, L., Yang, L., Peng, S., et al. (2023). Clinical and biological heterogeneities in triple-negative breast cancer reveals a non-negligible role of HER2-low. Breast Cancer Res *25*, 34. https://doi.org/10.1186/s13058-023-01639-y.

8. Castagnoli, L., Ladomery, M., Tagliabue, E., and Pupa, S.M. (2019). The d16HER2 Splice Variant: A Friend or Foe of HER2-Positive Cancers? Cancers (Basel) *11*, 902. https://doi.org/10.3390/cancers11070902.

9. Pedersen, K., Angelini, P.-D., Laos, S., Bach-Faig, A., Cunningham, M.P., Ferrer-Ramón, C., Luque-García, A., García-Castillo, J., Parra-Palau, J.L., Scaltriti, M., et al. (2009). A Naturally Occurring HER2 Carboxy-Terminal Fragment Promotes Mammary Tumor Growth and Metastasis. Molecular and Cellular Biology. https://doi.org/10.1128/MCB.01803-08.

10. Ginzel, J.D., Acharya, C.R., Lubkov, V., Mori, H., Boone, P.G., Rochelle, L.K., Roberts, W.L., Everitt, J.I., Hartman, Z.C., Crosby, E.J., et al. (2021). HER2 Isoforms Uniquely Program Intratumor Heterogeneity and Predetermine Breast Cancer Trajectories During the Occult Tumorigenic Phase. Molecular Cancer Research *19*, 1699–1711. https://doi.org/10.1158/1541-7786.MCR-21-0215.

11. Parra-Palau, J.L., Pedersen, K., Peg, V., Scaltriti, M., Angelini, P.D., Escorihuela, M., Mancilla, S., Sánchez Pla, A., Ramón y Cajal, S., Baselga, J., et al. (2010). A Major Role of p95/611-CTF, a Carboxy-Terminal Fragment of HER2, in the Down-modulation of the Estrogen Receptor in HER2-Positive Breast Cancers. Cancer Research *70*, 8537–8546. https://doi.org/10.1158/0008-5472.CAN-10-1701.

12. Parra-Palau, J.L., Morancho, B., Peg, V., Escorihuela, M., Scaltriti, M., Vicario, R., Zacarias-Fluck, M., Pedersen, K., Pandiella, A., Nuciforo, P., et al. (2014). Effect of p95HER2/611CTF on the Response to Trastuzumab and Chemotherapy. JNCI Journal of the National Cancer Institute *106*, dju291. https://doi.org/10.1093/jnci/dju291.

13. Starostecka, M., Jeong, H., Hasenfeld, P., Benito-Garagorri, E., Christiansen, T., Stober Brasseur, C., Gomes Queiroz, M., Garcia Montero, M., Jechlinger, M., and Korbel, J.O. (2025). Structural variant and nucleosome occupancy dynamics postchemotherapy in a HER2+ breast cancer organoid model. Proceedings of the National Academy of Sciences *122*, e2415475122. https://doi.org/10.1073/pnas.2415475122.

14. Scaltriti, M., Rojo, F., Ocana, A., Anido, J., Guzman, M., Cortes, J., Di Cosimo, S., Matias-Guiu, X., Ramon Y Cajal, S., Arribas, J., et al. (2007). Expression of p95HER2, a Truncated Form of the HER2 Receptor, and Response to Anti-HER2 Therapies in Breast Cancer. JNCI Journal of the National Cancer Institute *99*, 628–638. https://doi.org/10.1093/jnci/djk134.

15. Smith, L.M., Agar, J.N., Chamot-Rooke, J., Danis, P.O., Ge, Y., Loo, J.A., Paša-Tolić, L., Tsybin, Y.O., Kelleher, N.L., and THE CONSORTIUM FOR TOP-DOWN PROTEOMICS (2021). The Human Proteoform Project: Defining the human proteome. Science Advances *7*, eabk0734. https://doi.org/10.1126/sciadv.abk0734.

16. Sinha, A., Huang, V., Livingstone, J., Wang, J., Fox, N.S., Kurganovs, N., Ignatchenko, V., Fritsch, K., Donmez, N., Heisler, L.E., et al. (2019). The Proteogenomic Landscape of Curable Prostate Cancer. Cancer Cell *35*, 414-427.e6. https://doi.org/10.1016/j.ccell.2019.02.005.

17. Chatterjee, A., Rodger, E.J., and Eccles, M.R. (2018). Epigenetic drivers of tumourigenesis and cancer metastasis. Seminars in Cancer Biology *51*, 149–159. https://doi.org/10.1016/j.semcancer.2017.08.004.

18. Nguyen, D.X., and Massagué, J. (2007). Genetic determinants of cancer metastasis. Nat Rev Genet *8*, 341–352. https://doi.org/10.1038/nrg2101.

19. Iglesia, M.D., Jayasinghe, R.G., Chen, S., Terekhanova, N.V., Herndon, J.M., Storrs, E., Karpova, A., Zhou, D.C., Naser Al Deen, N., Shinkle, A.T., et al. (2024). Differential chromatin accessibility and transcriptional dynamics define breast cancer subtypes and their lineages. Nat Cancer *5*, 1713–1736. https://doi.org/10.1038/s43018-024-00773-6.

20. Chen, P., Zhang, X., Ding, R., Yang, L., Lyu, X., Zeng, J., Lei, J.H., Wang, L., Bi, J., Shao, N., et al. (2021). Patient-Derived Organoids Can Guide Personalized-Therapies for Patients with Advanced Breast Cancer. Advanced Science *8*, 2101176. https://doi.org/10.1002/advs.202101176.

21. Sanghi, A., Gruber, J.J., Metwally, A., Jiang, L., Reynolds, W., Sunwoo, J., Orloff, L., Chang, H.Y., Kasowski, M., and Snyder, M.P. (2021). Chromatin accessibility associates with protein-RNA correlation in human cancer. Nat Commun *12*, 5732. https://doi.org/10.1038/s41467-021-25872-1.

22. Chung, C.-Y., Ma, Z., Dravis, C., Preissl, S., Poirion, O., Luna, G., Hou, X., Giraddi, R.R., Ren, B., and Wahl, G.M. (2019). Single-Cell Chromatin Analysis of Mammary Gland Development Reveals Cell-State Transcriptional Regulators and Lineage Relationships. Cell Reports *29*, 495-510.e6. https://doi.org/10.1016/j.celrep.2019.08.089.

23. Hyeon, D.Y., Nam, D., Han, Y., Kim, D.K., Kim, G., Kim, D., Bae, J., Back, S., Mun, D.-G., Madar, I.H., et al. (2023). Proteogenomic landscape of human pancreatic ductal adenocarcinoma in an Asian population reveals tumor cell-enriched and immune-rich subtypes. Nat Cancer *4*, 290–307. https://doi.org/10.1038/s43018-022-00479-7.

24. Krug, K., Jaehnig, E.J., Satpathy, S., Blumenberg, L., Karpova, A., Anurag, M., Miles, G., Mertins, P., Geffen, Y., Tang, L.C., et al. (2020). Proteogenomic Landscape of Breast Cancer Tumorigenesis and Targeted Therapy. Cell *183*, 1436-1456.e31. https://doi.org/10.1016/j.cell.2020.10.036.

25. Buenrostro, J.D., Giresi, P.G., Zaba, L.C., Chang, H.Y., and Greenleaf, W.J. (2013). Transposition of native chromatin for fast and sensitive epigenomic profiling of open chromatin, DNA-binding proteins and nucleosome position. Nat Methods *10*, 1213–1218. https://doi.org/10.1038/nmeth.2688.

26. Swanson, E., Lord, C., Reading, J., Heubeck, A.T., Genge, P.C., Thomson, Z., Weiss, M.D., Li, X., Savage, A.K., Green, R.R., et al. (2021). Simultaneous trimodal single-cell measurement of transcripts, epitopes, and chromatin accessibility using TEA-seq. eLife *10*, e63632. https://doi.org/10.7554/eLife.63632.

27. Mimitou, E.P., Lareau, C.A., Chen, K.Y., Zorzetto-Fernandes, A.L., Hao, Y., Takeshima, Y., Luo, W., Huang, T.-S., Yeung, B.Z., Papalexi, E., et al. (2021). Scalable, multimodal profiling of chromatin accessibility, gene expression and protein levels in single cells. Nat Biotechnol *39*, 1246–1258. https://doi.org/10.1038/s41587-021-00927-2.

28. Chen, A.F., Parks, B., Kathiria, A.S., Ober-Reynolds, B., Goronzy, J.J., and Greenleaf, W.J. (2022). NEAT-seq: simultaneous profiling of intra-nuclear proteins, chromatin accessibility and gene expression in single cells. Nat Methods *19*, 547–553. https://doi.org/10.1038/s41592-022-01461-y.

29. Hughes, A.J., Spelke, D.P., Xu, Z., Kang, C.-C., Schaffer, D.V., and Herr, A.E. (2014). Single-cell western blotting. Nat Meth *11*, 749–755.

30. Kang, C.-C., Ward, T.M., Bockhorn, J., Schiffman, C., Huang, H., Pegram, M.D., and Herr, A.E. (2018). Electrophoretic cytopathology resolves ERBB2 forms with single-cell resolution. npj Precision Onc *2*, 1–10. https://doi.org/10.1038/s41698-018-0052-3.

31. Sinkala, E., Sollier-Christen, E., Renier, C., Rosàs-Canyelles, E., Che, J., Heirich, K., Duncombe, T.A., Vlassakis, J., Yamauchi, K.A., Huang, H., et al. (2017). Profiling protein expression in circulating tumour cells using microfluidic western blotting. Nat Commun *8*, 14622. https://doi.org/10.1038/ncomms14622.

32. Duncombe, T.A., Kang, C.-C., Maity, S., Ward, T.M., Pegram, M.D., Murthy, N., and Herr, A.E. (2016). Hydrogel Pore-Size Modulation for Enhanced Single-Cell Western Blotting. Advanced Materials *28*, 327–334. https://doi.org/10.1002/adma.201503939.

33. Gopal, A., and Herr, A.E. (2019). Multiplexed in-gel microfluidic immunoassays: characterizing protein target loss during reprobing of benzophenone-modified hydrogels. Sci Rep *9*, 15389. https://doi.org/10.1038/s41598-019-51849-8.

34. Subik, K., Lee, J.-F., Baxter, L., Strzepek, T., Costello, D., Crowley, P., Xing, L., Hung, M.-C., Bonfiglio, T., Hicks, D.G., et al. (2010). The Expression Patterns of ER, PR, HER2, CK5/6, EGFR, Ki-67 and AR by Immunohistochemical Analysis in Breast Cancer Cell Lines. Breast Cancer (Auckl) *4*, 117822341000400004. https://doi.org/10.1177/117822341000400004.

35. Abel, J., Jain, S., Rajan, D., Padigela, H., Leidal, K., Prakash, A., Conway, J., Nercessian, M., Kirkup, C., Javed, S.A., et al. (2024). AI powered quantification of nuclear morphology in cancers enables prediction of genome instability and prognosis. npj Precis. Onc. *8*, 134. https://doi.org/10.1038/s41698-024-00623-9.

36. Schöchlin, M., Weissinger, S.E., Brandes, A.R., Herrmann, M., Möller, P., and Lennerz, J.K. (2014). A nuclear circularity-based classifier for diagnostic distinction of desmoplastic from spindle cell melanoma in digitized histological images. Journal of Pathology Informatics *5*, 40. https://doi.org/10.4103/2153-3539.143335.

37. Eidet, J.R., Pasovic, L., Maria, R., Jackson, C.J., and Utheim, T.P. (2014). Objective assessment of changes in nuclear morphology and cell distribution following induction of apoptosis. Diagnostic Pathology *9*, 92. https://doi.org/10.1186/1746-1596-9-92.

38. Pienta, K.J., and Coffey, D.S. (1991). Correlation of nuclear morphometry with progression of breast cancer. Cancer *68*, 2012–2016. https://doi.org/10.1002/1097-0142(19911101)68:9%253C2012::AID-CNCR2820680928%253E3.0.CO;2-C.

39. Chen, X., Miragaia, R.J., Natarajan, K.N., and Teichmann, S.A. (2018). A rapid and robust method for single cell chromatin accessibility profiling. Nat Commun *9*, 5345. https://doi.org/10.1038/s41467-018-07771-0.

40. Rosenbluth, M.J., Lam, W.A., and Fletcher, D.A. (2008). Analyzing cell mechanics in hematologic diseases with microfluidic biophysical flow cytometry. Lab on a Chip *8*, 1010–1062. https://doi.org/10.1039/b802931h.

41. Chen, J.F., and Yan, Q. (2021). The roles of epigenetics in cancer progression and metastasis. Biochemical Journal *478*, 3373–3393. https://doi.org/10.1042/BCJ20210084.

42. He, Z., He, J., and Xie, K. (2023). KLF4 transcription factor in tumorigenesis. Cell Death Discov. *9*, 1–13. https://doi.org/10.1038/s41420-023-01416-y.

43. Hu, G., Pen, W., and Wang, M. (2019). TRIM14 Promotes Breast Cancer Cell Proliferation by Inhibiting Apoptosis. Oncol Res *27*, 439–447. https://doi.org/10.3727/096504018X15214994641786.

44. Ogunbolude, Y., Dai, C., Bagu, E.T., Goel, R.K., Miah, S., MacAusland-Berg, J., Ng, C.Y., Chibbar, R., Napper, S., Raptis, L., et al. (2017). FRK inhibits breast cancer cell migration

and invasion by suppressing epithelial-mesenchymal transition. Oncotarget *8*, 113034–113065. https://doi.org/10.18632/oncotarget.22958.

45. Scaltriti, M., Chandarlapaty, S., Prudkin, L., Aura, C., Jimenez, J., Angelini, P.D., Sánchez, G., Guzman, M., Parra, J.L., Ellis, C., et al. (2010). Clinical Benefit of Lapatinib-Based Therapy in Patients with Human Epidermal Growth Factor Receptor 2–Positive Breast Tumors Coexpressing the Truncated p95HER2 Receptor. Clinical Cancer Research *16*, 2688–2695. https://doi.org/10.1158/1078-0432.CCR-09-3407.

46. García-Castillo, J., Pedersen, K., Angelini, P.-D., Bech-Serra, J.J., Colomé, N., Cunningham, M.P., Parra-Palau, J.L., Canals, F., Baselga, J., and Arribas, J. (2009). HER2 Carboxyl-terminal Fragments Regulate Cell Migration and Cortactin Phosphorylation *. Journal of Biological Chemistry *284*, 25302–25313. https://doi.org/10.1074/jbc.M109.001982.

47. O'Neill, F., Madden, S.F., Aherne, S.T., Clynes, M., Crown, J., Doolan, P., and O'Connor, R. (2012). Gene expression changes as markers of early lapatinib response in a panel of breast cancer cell lines. Molecular Cancer *11*, 41. https://doi.org/10.1186/1476-4598-11-41.

48. Burris, H.A., Hurwitz, H.I., Dees, E.C., Dowlati, A., Blackwell, K.L., O'Neil, B., Marcom, P.K., Ellis, M.J., Overmoyer, B., Jones, S.F., et al. (2005). Phase I Safety, Pharmacokinetics, and Clinical Activity Study of Lapatinib (GW572016), a Reversible Dual Inhibitor of Epidermal Growth Factor Receptor Tyrosine Kinases, in Heavily Pretreated Patients With Metastatic Carcinomas. JCO *23*, 5305–5313. https://doi.org/10.1200/JCO.2005.16.584.

49. Gayle, S.S., Arnold, S.L.M., O'Regan, R.M., and Nahta, R. Pharmacologic Inhibition of mTOR Improves Lapatinib Sensitivity in HER2-Overexpressing Breast Cancer Cells with Primary Trastuzumab Resistance. Anti-Cancer Agents in Medicinal Chemistry *12*, 151–162. https://doi.org/10.2174/187152012799015002.

50. Brady, S.W., Zhang, J., Tsai, M.-H., and Yu, D. (2015). PI3K-independent mTOR activation promotes lapatinib resistance and IAP expression that can be effectively reversed by mTOR and Hsp90 inhibition. Cancer Biology & Therapy *16*, 402–411. https://doi.org/10.1080/15384047.2014.1002693.

51. Deng, J., Ji, Y., Zhu, F., Liu, L., Li, L., Bai, X., Li, H., Liu, X., Luo, Y., Lin, B., et al. (2022). Mapping secretome-mediated interaction between paired neuron–macrophage single cells. Proceedings of the National Academy of Sciences *119*, e2200944119. https://doi.org/10.1073/pnas.2200944119.

52. Cyr, A.R., Kulak, M.V., Park, J.M., Bogachek, M.V., Spanheimer, P.M., Woodfield, G.W., White-Baer, L.S., O'Malley, Y.Q., Sugg, S.L., Olivier, A.K., et al. (2015). TFAP2C Governs the Luminal Epithelial Phenotype in Mammary Development and Carcinogenesis. Oncogene *34*, 436–444. https://doi.org/10.1038/onc.2013.569.

53. Tewey, K.M., Rowe, T.C., Yang, L., Halligan, B.D., and Liu, L.F. (1984). Adriamycin-Induced DNA Damage Mediated by Mammalian DNA Topoisomerase II. Science *226*, 466–468. https://doi.org/10.1126/science.6093249.

54. Qiao, X., van der Zanden, S.Y., Wander, D.P.A., Borràs, D.M., Song, J.-Y., Li, X., van Duikeren, S., van Gils, N., Rutten, A., van Herwaarden, T., et al. (2020). Uncoupling DNA damage from chromatin damage to detoxify doxorubicin. Proceedings of the National Academy of Sciences *117*, 15182–15192. https://doi.org/10.1073/pnas.1922072117.

55. Pang, B., Qiao, X., Janssen, L., Velds, A., Groothuis, T., Kerkhoven, R., Nieuwland, M., Ovaa, H., Rottenberg, S., van Tellingen, O., et al. (2013). Drug-induced histone eviction from open chromatin contributes to the chemotherapeutic effects of doxorubicin. Nat Commun *4*, 1908. https://doi.org/10.1038/ncomms2921.

56. Chen, X., Zhao, W., Huang, Y., Luo, S., Tang, X., and Yi, Q. (2024). Association of GATA3 expression in triple-positive breast cancer with overall survival and immune cell infiltration. Sci Rep *14*, 17795. https://doi.org/10.1038/s41598-024-68788-8.

57. Saha, S.K., Islam, S.M.R., Saha, T., Nishat, A., Biswas, P.K., Gil, M., Nkenyereye, L., El-Sappagh, S., and Cho, M.S.I.& S.-G. (2021). Prognostic role of EGR1 in breast cancer: a systematic review. BMB Reports *54*, 497–504. https://doi.org/10.5483/BMBRep.2021.54.10.087.

58. Zhou, Z., Qiu, R., Liu, W., Yang, T., Li, G., Huang, W., Teng, X., Yang, Y., Yu, H., Yang, Y., et al. (2021). BCAS3 exhibits oncogenic properties by promoting CRL4A-mediated ubiquitination of p53 in breast cancer. Cell Proliferation *54*, e13088. https://doi.org/10.1111/cpr.13088.

59. Laska, M.J., Lowe, S.W., Zender, L., Hearn, S., Vogel, U., Jensen, U.B., Bric, A., and Nexø, B.A. (2009). Enforced expression of PPP1R13L increases tumorigenesis and invasion through p53-dependent and p53-independent mechanisms. Molecular Carcinogenesis *48*, 832–842. https://doi.org/10.1002/mc.20528.

60. Rosenbluth, J.M., Schackmann, R.C.J., Gray, G.K., Selfors, L.M., Li, C.M.-C., Boedicker, M., Kuiken, H.J., Richardson, A., Brock, J., Garber, J., et al. (2020). Organoid cultures from normal and cancer-prone human breast tissues preserve complex epithelial lineages. Nat Commun *11*, 1711. https://doi.org/10.1038/s41467-020-15548-7.

61. Neve, R.M., Chin, K., Fridlyand, J., Yeh, J., Baehner, F.L., Fevr, T., Clark, L., Bayani, N., Coppe, J.P., Tong, F., et al. (2006). A collection of breast cancer cell lines for the study of functionally distinct cancer subtypes. Cancer Cell *10*, 515–527. https://doi.org/10.1016/j.ccr.2006.10.008.

62. Duchnowska, R., Sperinde, J., Czartoryska-Arłukowicz, B., Myśliwiec, P., Winslow, J., Radecka, B., Petropoulos, C., Demlova, R., Orlikowska, M., Kowalczyk, A., et al. (2017). Predictive value of quantitative HER2, HER3 and p95HER2 levels in HER2-positive advanced breast cancer patients treated with lapatinib following progression on trastuzumab. Oncotarget *8*, 104149–104159. https://doi.org/10.18632/oncotarget.22027.

63. Han, S.-W., Cha, Y., Paquet, A., Huang, W., Weidler, J., Lie, Y., Sherwood, T., Bates, M., Haddad, M., Park, I.H., et al. (2012). Correlation of HER2, p95HER2 and HER3 Expression

and Treatment Outcome of Lapatinib plus Capecitabine in her2-Positive Metastatic Breast Cancer. PLOS ONE *7*, e39943. https://doi.org/10.1371/journal.pone.0039943.

64. Moliterni, A., Ménard, S., Valagussa, P., Biganzoli, E., Boracchi, P., Balsari, A., Casalini, P., Tomasic, G., Marubini, E., Pilotti, S., et al. (2003). HER2 Overexpression and Doxorubicin in Adjuvant Chemotherapy for Resectable Breast Cancer. JCO *21*, 458–462. https://doi.org/10.1200/JCO.2003.04.021.

65. Campiglio, M., Somenzi, G., Olgiati, C., Beretta, G., Balsari, A., Zaffaroni, N., Valagussa, P., and Ménard, S. (2003). Role of proliferation in HER2 status predicted response to doxorubicin. International Journal of Cancer *105*, 568–573. https://doi.org/10.1002/ijc.11113.

66. Gennari, A., Sormani, M.P., Pronzato, P., Puntoni, M., Colozza, M., Pfeffer, U., and Bruzzi, P. (2008). HER2 Status and Efficacy of Adjuvant Anthracyclines in Early Breast Cancer: A Pooled Analysis of Randomized Trials. JNCI: Journal of the National Cancer Institute *100*, 14–20. https://doi.org/10.1093/jnci/djm252.

67. Espelin, C.W., Leonard, S.C., Geretti, E., Wickham, T.J., and Hendriks, B.S. (2016). Dual HER2 Targeting with Trastuzumab and Liposomal-Encapsulated Doxorubicin (MM-302) Demonstrates Synergistic Antitumor Activity in Breast and Gastric Cancer. Cancer Research *76*, 1517–1527. https://doi.org/10.1158/0008-5472.CAN-15-1518.

68. Ding, Y., Ding, K., He, X., Mo, W., Liang, C., Gong, L., Huang, Y., and Ding, X. (2023). The Value of Neoadjuvant Anthracycline-Based Regimens for HER2-Positive Breast Cancer: A Systematic Review and Meta-analysis Including 1366 Patients. Clin Med Insights Oncol *17*, 11795549231195293. https://doi.org/10.1177/11795549231195293.

69. Deviri, D., and Safran, S.A. (2022). Balance of osmotic pressures determines the nuclear-to-cytoplasmic volume ratio of the cell. Proceedings of the National Academy of Sciences *119*, e2118301119. https://doi.org/10.1073/pnas.2118301119.

70. Scott, N.R., Kang, S., and Parekh, S.H. (2024). Mechanosensitive nuclear uptake of chemotherapy. Sci Adv *10*, eadr5947. https://doi.org/10.1126/sciadv.adr5947.

71. Sinha, A., Huang, V., Livingstone, J., Wang, J., Fox, N.S., Kurganovs, N., Ignatchenko, V., Fritsch, K., Donmez, N., Heisler, L.E., et al. (2019). The Proteogenomic Landscape of Curable Prostate Cancer. Cancer Cell *35*, 414-427.e6. https://doi.org/10.1016/j.ccell.2019.02.005.

72. Wang, J., Zibetti, C., Shang, P., Sripathi, S.R., Zhang, P., Cano, M., Hoang, T., Xia, S., Ji, H., Merbs, S.L., et al. (2018). ATAC-Seq analysis reveals a widespread decrease of chromatin accessibility in age-related macular degeneration. Nat Commun *9*, 1364. https://doi.org/10.1038/s41467-018-03856-y.

73. Tsou, P.-S., Palisoc, P.J., Ali, M., Khanna, D., and Sawalha, A.H. (2021). Genome-Wide Reduction in Chromatin Accessibility and Unique Transcription Factor Footprints in

Endothelial Cells and Fibroblasts in Scleroderma Skin. Arthritis & Rheumatology *73*, 1501–1513. https://doi.org/10.1002/art.41694.

74. Sachs, N., de Ligt, J., Kopper, O., Gogola, E., Bounova, G., Weeber, F., Balgobind, A.V., Wind, K., Gracanin, A., Begthel, H., et al. (2018). A Living Biobank of Breast Cancer Organoids Captures Disease Heterogeneity. Cell *172*, 373-386.e10. https://doi.org/10.1016/j.cell.2017.11.010.

75. Yang, F., Wang, Y., Li, Q., Cao, L., Sun, Z., Jin, J., Fang, H., Zhu, A., Li, Y., Zhang, W., et al. (2017). Intratumor heterogeneity predicts metastasis of triple-negative breast cancer. Carcinogenesis *38*, 900–909. https://doi.org/10.1093/carcin/bgx071.

76. Mülhardt, C. (2013). Untersuchung der Funktion von DNA-Sequenzen. In Der Experimentator Molekularbiologie/Genomics, C. Mülhardt, ed. (Springer), pp. 211–268. https://doi.org/10.1007/978-3-642-34636-1_9.

77. Dekkers, J.F., van Vliet, E.J., Sachs, N., Rosenbluth, J.M., Kopper, O., Rebel, H.G., Wehrens, E.J., Piani, C., Visvader, J.E., Verissimo, C.S., et al. (2021). Long-term culture, genetic manipulation and xenotransplantation of human normal and breast cancer organoids. Nat Protoc *16*, 1936–1965. https://doi.org/10.1038/s41596-020-00474-1.

78. Kang, C.-C., Yamauchi, K.A., Vlassakis, J., Sinkala, E., Duncombe, T.A., and Herr, A.E. (2016). Single cell–resolution western blotting. Nat Protoc *11*, 1508–1530. https://doi.org/10.1038/nprot.2016.089.

79. Gopal, A., and Herr, A.E. (2021). Segmentation-based analysis of single-cell immunoblots. Electrophoresis *42*, 2070–2080. https://doi.org/10.1002/elps.202100144.

80. Ducret, A., Quardokus, E.M., and Brun, Y.V. (2016). MicrobeJ, a tool for high throughput bacterial cell detection and quantitative analysis. Nat Microbiol *1*, 16077. https://doi.org/10.1038/nmicrobiol.2016.77.

81. Kochetov, B., Bell, P.D., Garcia, P.S., Shalaby, A.S., Raphael, R., Raymond, B., Leibowitz, B.J., Schoedel, K., Brand, R.M., Brand, R.E., et al. (2024). UNSEG: unsupervised segmentation of cells and their nuclei in complex tissue samples. Commun Biol *7*, 1062. https://doi.org/10.1038/s42003-024-06714-4.

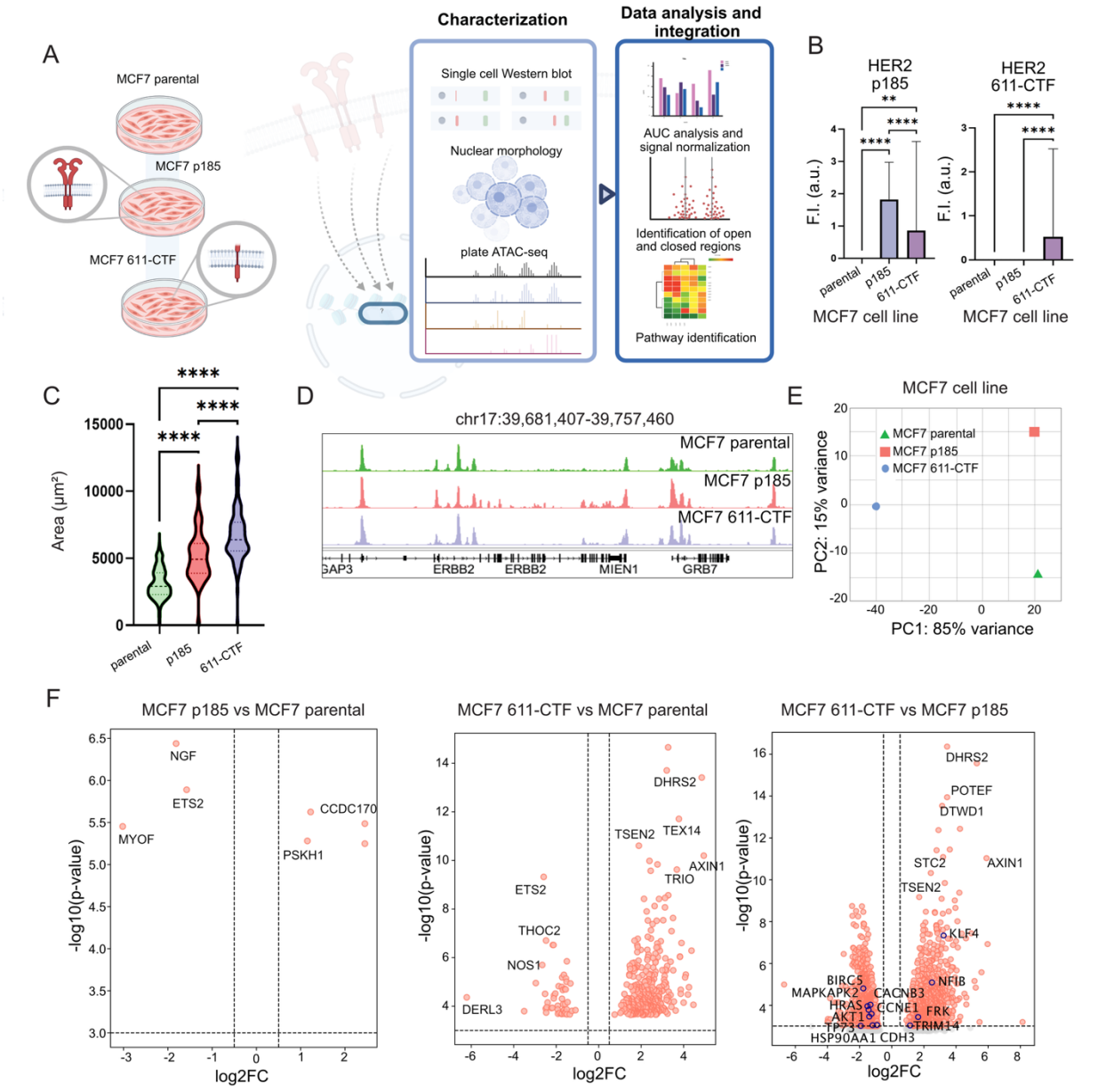

Figure 1. The presence of HER2 611-CTF alters chromatin accessibility more substantially than increased abundance of p185 proteoform.

A) Schematic of the study. Three transfected cell lines with HER2 proteoforms (empty vector -parental-, full-length HER2 form p185, and truncated proteoform 611-CTF) are evaluated for the changes in chromatin accessibility, protein expression, and nuclei morphology.

B) Bar plot showing HER2 p185 (left) and 611-CTF (right) expression across the transfected cell lines, confirming that MCF7 p185 present only p185 expression, while MCF7 611-CTF have expression of both full-length and fragment protein. F.I. corresponds to fluorescence intensity and a.u. to arbitrary units.

*C) Comparison of nucleus area between the three cell lines, with the area of cells expressing the 611-CTF fragment significantly increasing in comparison with the other conditions. Significance: * $P \leq 0.05$, ** $P \leq 0.01$, *** $P \leq 0.001$, **** $P \leq 0.0001$.*

D) Changes in chromatin accessibility at the ERBB2 gene in MCF7 parental, p185, and 611-CTF cell lines. Genome browser tracks (GRCh38) show chromatin accessibility at the ERBB2 (HER2), MIEN1, and GRB7 gene loci in MCF7-transfected cell lines. Differentially accessible (DA) peaks are enriched in the ERBB2 region in the full-length HER2 (p185) sample, while DA peaks in GRB7 are observed in both p185 and 611-CTF HER2-expressing cell lines. All track lines have the same y-axis limits, and peak heights are scaled across all samples.

E) Principal Component Analysis (PCA) of ATAC-seq signal in the three MCF7-transfected cell lines. The PCA plot shows sample clustering based on chromatin accessibility variation. PC1 (85% variance) separates p185 (red) and parental MCF7 (green), while 611-CTF (blue) clusters separately from both, indicating a distinct chromatin accessibility profile compared to the other conditions.

F) Volcano plots of ATAC-seq peaks comparing p185 vs. parental MCF7s (left), 611-CTF vs. parental MCF7 (middle), and 611-CTF vs. p185 (right). Peaks with significantly differential chromatin accessibility are highlighted in red, while the non-significant peaks are grey. The vertical dotted line represents an absolute log2 fold change of 1.0, while the horizontal dotted line represents an adjusted p-value threshold of 0.00001. FDR-corrected p-values were obtained using DESeq2.

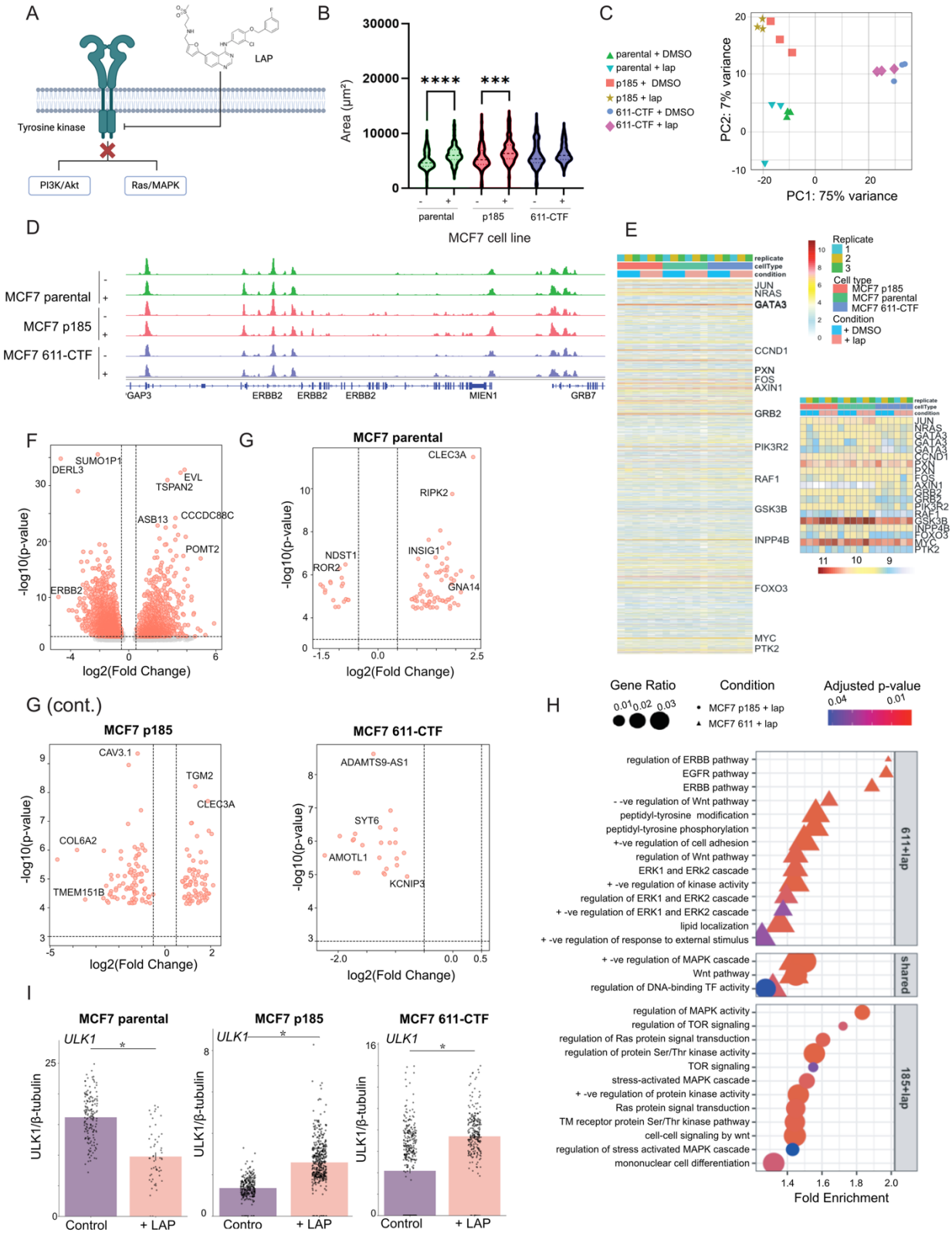

Figure 2. Lapatinib treatment leads to modest changes in chromatin.

A) Scheme representing the mechanism of action of lapatinib (LAP). Lapatinib inhibits the tyrosine kinase domain of HER2, inhibiting PI3K/Akt and Ras/MAPK pathways[2].

*B) Changes in nuclei area after lapatinib treatment. The area significantly increased in MCF7 parental and p185. Significance is as follows: * $P \leq 0.05$, ** $P \leq 0.01$, *** $P \leq 0.001$, **** $P \leq 0.0001$.*

C) PCA of chromatin accessibility in MCF7 cell lines (parental, p185, and 611-CTF) treated with lapatinib (lap) or control (DMSO). PC1 (75% variance) separates 611-CTF from p185 and parent, indicating distinct chromatin accessibility profiles between these HER2 proteoforms. PC2 (7% variance) captures minimal variation due to treatment, suggesting that lapatinib induces only subtle chromatin accessibility changes in p185 and parent cells. MCF7 611-CTF shows no clear separation between lap-treated and control conditions, indicating a lack of response at the chromatin level. Overall, cell line identity is the primary driver of variation, while lapatinib treatment has a minimal effect on chromatin accessibility.

D) Changes in chromatin accessibility at the ERBB2 gene in MCF7 parental, p185, and 611-CTF cell lines with (+) and without (-) lapatinib treatment. Genome browser tracks (GRCh38) show chromatin accessibility at the ERBB2 (HER2), MIEN1, and GRB7 gene loci in MCF7-transfected cell lines with and without lapatinib treatment. Lapatinib show minimal to no effect between the rearment in each cell line. All track lines have the same y-axis limits, and peak heights are scaled across all samples.

E) Heatmap of chromatin accessibility in 100 key breast cancer-related genes across MCF7-derived cell lines (parental, p185, and 611-CTF) treated with lapatinib (lap) or control (DMSO). Data were Z-score normalized per gene (row normalization) to highlight relative accessibility changes. A subset heatmap zooms in on regions with at least one condition exceeding a Z-score of 9.5, with further scaling applied to enhance visualization.

F) Volcano plot of differentially accessible chromatin regions between MCF7 611-CTF and MCF7 p185 cell lines under lapatinib (lap) treatment. Each point represents a chromatin region, with red indicating significant changes (FDR-adjusted p-value < 0.00001). The x-axis (Log_2 fold change) shows regions more accessible in p185 (left) or 611-CTF (right), while the y-axis ($-log_{10}$ p-value) represents significance.

G) Volcano plots of differentially accessible chromatin regions between lapatinib-treated (lap) and control (DMSO) conditions in parental, p185, and 611-CTF MCF7 cell lines. Each point represents a chromatin region, with red indicating significant changes (FDR-adjusted p-value < 0.0001). The x-axis (Log_2 fold change) shows regions more accessible in control (left) or lap-treated (right), while the y-axis ($-log_{10}$ p-value) represents significance. Lapatinib induces minimal chromatin accessibility changes across all cell lines, with p185 showing the strongest response and 611-CTF exhibiting the weakest. The vertical dotted line represents an absolute log2 fold change of 1.0, while the horizontal dotted line represents an adjusted p-value threshold of 0.00001. FDR-corrected p-values were obtained using DESeq2.

G) PCA analysis of protein expression decided based on the highest log2Fold common across the three cell lines (ULK1, TFAP2, HER2, and the housekeeping protein TUBB3. Only MCF7 parental

cells showed separation after lapatinib treatment, while p185 and 611-CTF remain largely unchanged.

H) Gene Ontology (GO) enrichment analysis of differentially accessible chromatin regions in 611-CTF (611lap) and p185 (185lap) cell lines under lapatinib treatment. Enriched pathways are categorized into those specific to 611lap (top panel), shared between both cell lines (middle panel), and specific to 185lap (bottom panel). The x-axis represents fold enrichment, while the y-axis lists significantly enriched GO terms. Dot size corresponds to the gene ratio, and color indicates the adjusted p-value, with red representing the most significant pathways. For brevity on y-axis labels, 'positive' is abbreviated as "+-*ve*", and negative is abbreviated as " - -*ve*".

I) Bar plot showing ULK1 expression increase after lapatinib treatment in MCF7 p185 and 611-CTF, while showing a significant decrease in MCF7 parental cells.

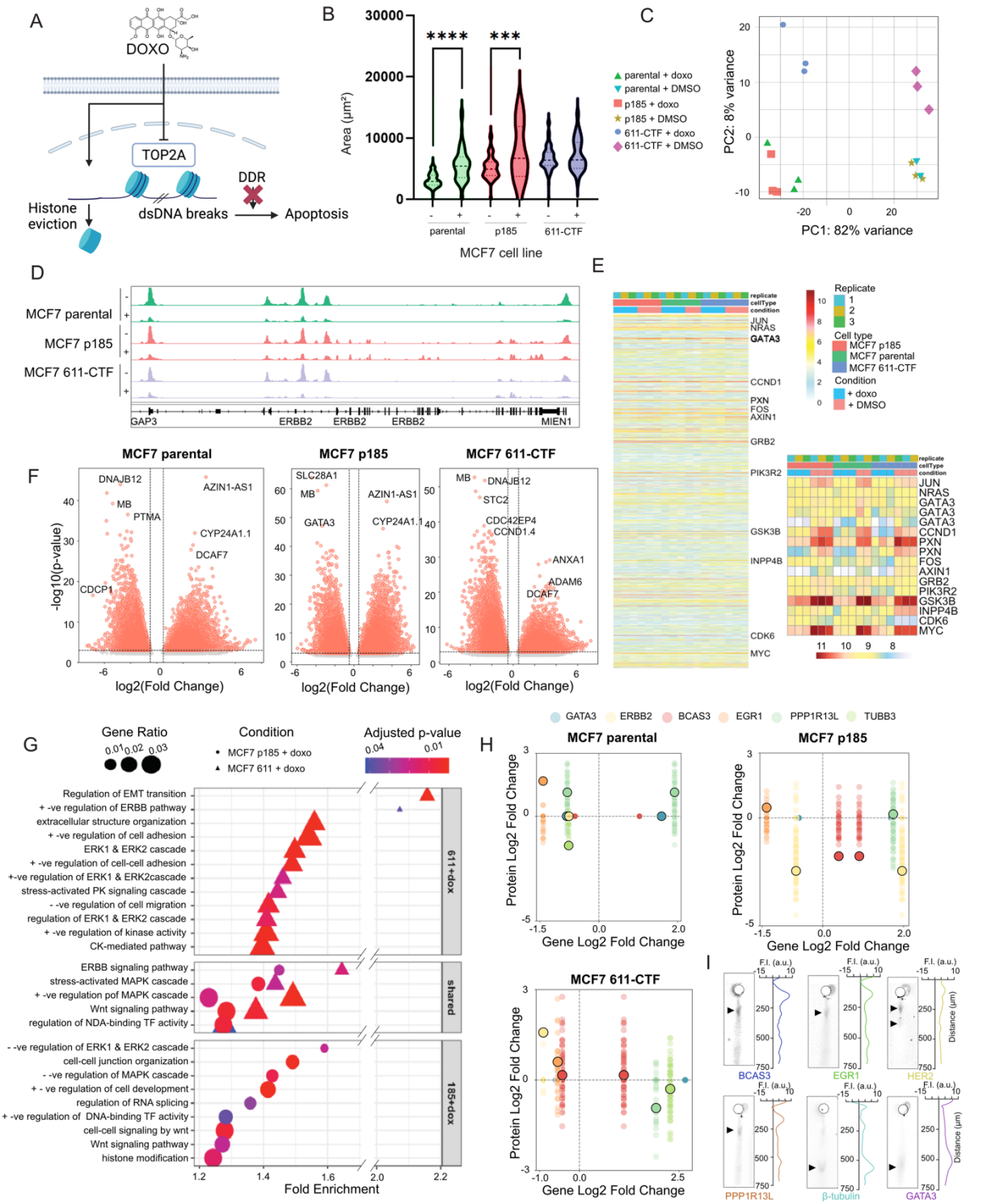

Figure 3. Doxorubicin treatment induces widespread changes in chromatin accessibility across all cell types.

A) Scheme showing the mechanism of action of doxorubicin (DOXO) on the chromatin of the cells[1]*. DDR: DNA damage response.*

*B) Violin plot showing changes in nuclei area after doxorubicin treatment, which significantly increases in MCF7 parental and MCF7 p185. Significance: * $P \leq 0.05$, ** $P \leq 0.01$, *** $P \leq 0.001$, **** $P \leq 0.0001$.*

C) PCA of ATAC-seq signal in MCF7-derived cell lines treated with doxorubicin (doxo) or control (DMSO). PC1 (82% variance) primarily separates doxo-treated from control samples, indicating that doxo treatment is the major driver of chromatin accessibility changes. PC2 (8% variance) captures additional variation, likely reflecting differences between cell lines. p185+doxo (red) and parental+doxo (green) cluster closely together, suggesting a similar chromatin accessibility response to doxorubicin. In contrast, 611-CTF+doxo (blue) clusters separately, indicating a distinct chromatin remodeling response compared to p185 and parental under doxorubicin treatment.

D) Changes in chromatin accessibility at the ERBB2 gene in MCF7 parental, p185, and 611-CTF cell lines with (+) and without (-) doxo treatment. Genome browser tracks (GRCh38) show chromatin accessibility at the ERBB2 (HER2) and MIEN1 gene loci in MCF7-transfected cell lines with and without doxo. Differentially accessible (DA) peaks are suppressed in the ERBB2 and MIEN1 region in all doxo-treated samples compared to control samples within the cell lines. All track lines have the same y-axis limits, and peak heights are scaled across all samples.

E) Heatmap of differential chromatin accessibility in key breast cancer-related genes across MCF7-derived cell lines (parent, p185, and 611-CTF) treated with doxo or control. Data were Z-score normalized per gene (row normalization) to highlight relative accessibility changes. Doxo treatment results in widespread chromatin closure, with MYC, PXN, AXIN1, JUN, GATA3, and CCND1 showing reduced accessibility across all cell lines. Samples are clustered based on chromatin accessibility, with colors representing Z-scores (red = increased accessibility, blue = decreased accessibility).

F) Volcano plots showing differentially accessible chromatin regions between doxo-treated and control conditions in parent, p185, and 611-CTF MCF7-derived cell lines. Each point represents an individual chromatin region, with red indicating significantly differentially accessible regions (FDR-adjusted p-value < 0.001) and grey representing nonsignificant regions. The x-axis (Log_2 fold change) indicates accessibility changes, where negative values (left) represent regions more accessible in control, and positive values (right) represent regions more accessible in doxo-treated samples. The vertical dotted line represents an absolute log2 fold change of 0.5, while the horizontal dotted line represents an adjusted p-value threshold of 0.001. FDR-corrected p-values were obtained using DESeq2.

G) GO enrichment analysis of differentially accessible chromatin regions in doxorubicin-treated MCF7 p185 (185+doxo) and MCF7 611-CTF (611+doxo) cell lines. Enriched pathways are categorized into those specific to 611+doxo (top panel), shared between MCF7 611+doxo and MCF7 185+doxo (middle panel), and specific to 185+doxo (bottom panel). The x-axis represents fold enrichment, while the y-axis lists significantly enriched GO terms. Dot size corresponds to the gene ratio, and color indicates the adjusted p-value, with red representing the most significant pathways (lowest p-value). The word positive was shortened as + -ve, and negative is - -ve.

H) Scatterplot of Protein Log2 fold change and gene Log2 fold change after doxo treatment. Circle with a dark outline represents the average Log2 fold change across all the tested single cells.

I) Single-cell Western blot of selected proteins in MCF7 611-CTFcells after doxo treatment. False-color micrographs show the protein location, with companion intensity trace at the right side of each. F.I. corresponds to fluorescence intensity.

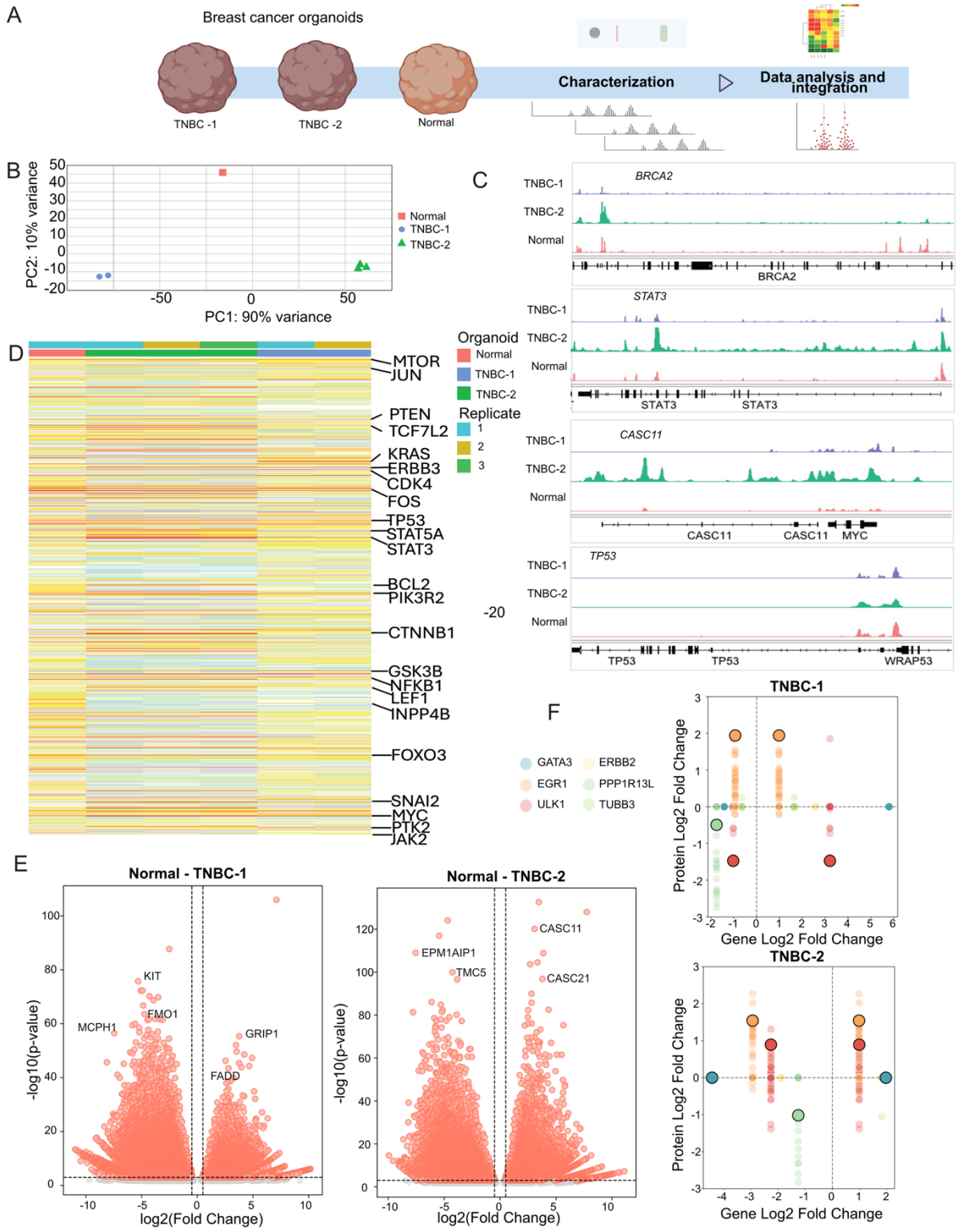

Figure 4. Chromatin accessibility and HER2 protein expression in TNBC patient-derived organoids. *A) Schematic representation of triple-negative breast cancer (TNBC) organoids derived from Grade 2 (TNBC-2) and Grade 3 (TNBC-1) human tumors, alongside a normal human*

breast tissue organoid (Normal). The workflow includes protein characterization, chromatin accessibility profiling, and integrative data analysis.
B) PCA of chromatin accessibility in the tested organoids. PC1 (90% variance) primarily separates the organoids, indicating major chromatin accessibility differences. TNBC-1 (blue) is the most distinct, clustering farthest from the others, suggesting a highly altered chromatin landscape. TNBC-2 (green) is the most similar within its group, forming a tight cluster on the right. Normal (red) is intermediate, positioned separately along PC2 (10% variance), suggesting greater variability compared to TNBC-2 but less distinct than TNBC-1. The strong PC1 separation highlights major epigenetic differences among these TNBC organoid models.
C) Genome browser tracks showing chromatin accessibility profiles at key breast cancer-associated loci (BRCA2, STAT3, CASC11, MYC, TP53, and WRAP53) across TNBC-1, TNBC-2, and Normal.
D) Heatmap of chromatin accessibility across key signaling genes in TNBC organoids and normal controls. Each row represents a genomic region, with color intensity reflecting accessibility levels (Z-score normalized). Warmer colors (red/yellow) indicate higher accessibility, while cooler colors (blue/green) represent lower accessibility. Annotated regions with Z-score > 9.5 are labeled, highlighting regions with extreme chromatin accessibility changes.
E) Volcano plots of differentially accessible chromatin regions in TNBC-2 (left) and TNBC-1 (right), using Normal as the reference. Each point represents a chromatin region, with red indicating significant changes (FDR-adjusted p-value < 0.001).
F) Protein log2Fold change compared to gene log2Fold change of TNBC-1 and TNBC-2 using Normal as reference. Circle with a dark outline represents the average log2fold across all the tested single cells.

References

1. Pang, B., Qiao, X., Janssen, L., Velds, A., Groothuis, T., Kerkhoven, R., Nieuwland, M., Ovaa, H., Rottenberg, S., van Tellingen, O., et al. (2013). Drug-induced histone eviction from open chromatin contributes to the chemotherapeutic effects of doxorubicin. Nat Commun *4*, 1908. https://doi.org/10.1038/ncomms2921.

2. Segovia-Mendoza, M., González-González, M.E., Barrera, D., Díaz, L., and García-Becerra, R. (2015). Efficacy and mechanism of action of the tyrosine kinase inhibitors gefitinib, lapatinib and neratinib in the treatment of HER2-positive breast cancer: preclinical and clinical evidence. Am J Cancer Res *5*, 2531–2561.